ESC-TR-99-059

Technical Report
1056

Multisensor Fusion Processing for Enhanced Radar Imaging

L.D. Vann
K.M. Cuomo
J.E. Piou
J.T. Mayhan

5 April 2000

Lincoln Laboratory

MASSACHUSETTS INSTITUTE OF TECHNOLOGY

LEXINGTON, MASSACHUSETTS

Prepared for the Department of the Army
under Air Force Contract F19628-95-C-0002.

Approved for public release; distribution is unlimited.

This report is based on studies performed at Lincoln Laboratory, a center for research operated by Massachusetts Institute of Technology. The work was sponsored by the U.S. Army Space & Missile Defense Command under Air Force Contract F19628-95-C-0002.

This technical report has been reviewed and is approved for publication.

FOR THE COMMANDER

Gary Tutungian
Administrative Contracting Officer
Plans and Programs Directorate
Contracted Support Management

MASSACHUSETTS INSTITUTE OF TECHNOLOGY
LINCOLN LABORATORY

MULTISENSOR FUSION PROCESSING FOR ENHANCED RADAR IMAGING

L.D. VANN
K.M. CUOMO
J.E. PIOU
J.T. MAYHAN
Group 34

TECHNICAL REPORT 1056

5 APRIL 2000

LEXINGTON MASSACHUSETTS

ABSTRACT

This report considers the problem of fusing signature data from a variety of sensors operating over different frequency bands and interrogating a target over diverse angular positions. In particular, the report develops (1) a framework for fusing signature data for this diverse operating scenario, (2) candidate sensor-fusion algorithms, and (3) a general formulation characterizing the practical problem of cohering data associated with multiband spatially distributed sensors. The report illustrates the formulation by considering numerous examples, transitioning from simple illustrative targets to progressively more difficult and physically realistic targets. The report begins with a constant-amplitude point-scatter model, progresses to three-dimensional targets, and ends by illustrating enhanced image-fusion algorithms applied to static-range data.

This report can be considered a complement to the ultrawide-bandwidth development presented in [1], which develops the general formulation for fusing signature data from sparse-band collocated sensors. The report focuses primarily on the complementary problem of sparse-angle sensor fusion, where three main effects complicate the fusion process: specular responses, diffraction from discontinuities, and shadowing. These effects prohibit the use of a constant-amplitude point-scatter model for characterizing the target over broad angular regions.

TABLE OF CONTENTS

LIST OF ILLUSTRATIONS

LIST OF ILLUSTRATIONS (Continued)

1. INTRODUCTION

1.1 OVERVIEW

There is considerable interest within the ballistic missile defense community for the various theater and area defense systems to operate as a family of systems. A key ingredient in fully accomplishing this objective is the capability to fuse signature data from a variety of sensors operating over different frequency bands and interrogating a target over diverse angular positions. This report develops (1) a framework for fusing signature data for this diverse operating scenario, (2) candidate sensor-fusion algorithms, and (3) a general formulation characterizing the practical problem of cohering data associated with multiband spatially distributed sensors. The report illustrates the formulation by considering numerous examples, transitioning from simple illustrative targets to progressively more difficult and physically realistic targets. The report begins with a constant-amplitude point-scatter model, progresses to three-dimensional targets, and ends by illustrating enhanced image-fusion algorithms applied to static-range data.

Many different measures might be used to quantify the enhancements gained from fusing signature data; this report considers using an image processor to combine radar cross section data from multispectral distributed sensors whose frequency bands and angular coverage may or may not overlap. The image that results provides a higher degree of spatial resolution than would be available from each sensor independently. This enhanced image might then be used in subsequent processing to identify and characterize specific features on the target. Limitations to using the conventional image integral as the data-fusion processor are also discussed, and enhanced imaging techniques are developed to provide improved results.

This report can be considered a complement to the ultrawide-bandwidth development presented in [1], which develops the general formulation for fusing signature data from sparse-band collocated sensors. This report focuses primarily on the complementary problem of sparse-angle sensor fusion, where three main effects complicate the fusion process: specular responses, diffraction from discontinuities, and shadowing. These effects prohibit the use of a constant-amplitude point-scatter model for characterizing the target over broad angular regions.

Section 1.2 introduces the motivation for this study and discusses what components must be included in an image processor in order to obtain the best-possible image from multisensor signature data. Section 2 reviews some concepts related to imaging as a data-fusion mechanism, such as proper data formatting to obtain properly focused images and the proper construction of the image using conventional image-processing techniques. Section 3 addresses data coherence and compensation for the contaminated data that result from spatially separated and sparse-band sensors; a general procedure is developed for cohering sparse-band, sparse-angle data from separate sensors. The coherence technique developed in [1] for sparse-band collocated sensors is extended to the more general case, and a striking duality is developed between cohering sparse-band collocated sensors and sparse-angle narrowband sensors. Section 4 demonstrates results for several types of targets, ranging from a constant-amplitude point-scatter model to a three-dimensional canonical shape, and demonstrates the practicability of these techniques using static-range data from a canonical target of interest. To effect sparse-angle fusion, a new basis-expansion set is introduced that employs a localized all-pole model over a limited angular sector and then uses this basis set for fusing the data between angularly spaced sectors. Examples of preprocessing data for mutual coherence and multidimensional ultrawide-bandwidth processing are considered in Section 5.

1.2 MOTIVATION

The increased target resolution of today's wideband radar systems has significantly improved the capability of ballistic missile defense systems for real-time discrimination and target identification. Advanced signal-processing methods have further improved the resolution achievable from processed radar returns. The extension of these techniques to coherent combination of data from multiple sensors operating over different frequency bands is discussed in [1]; in particular, an algorithm was developed that could compensate for the lack of mutual coherence between radars operating independently over sparsely located subbands, allowing for the fusion of multisensor data to obtain an ultrawide-bandwidth characterization of the target in track. This algorithm has been exploited in considerable detail for nearly collocated sensors; this report considers this fusion process for sensors that are sparsely located in angle.

Concomitant with these processing developments, the ballistic missile defense community has shown considerable interest in the various theater- and area-defense systems operating as a family of systems. Joint operation of these sensors can take on several levels of complexity, as illustrated in Figure 1. This figure defines a hierarchy of possible jointness functions, beginning with the simplest and evolving to more sophisticated fusion processes. The hierarchy indicated by "function of jointness" might be as simple as sharing intelligence data or combining tracks from multiple sensors in order to provide a more accurate target cue, or might be as complex as correlating and/or combining radar cross section (signature) data in order to share target and identification features and/or to coordinate engagement decisions. This last, the highest function of jointness in this hierarchy, is addressed in this report: integrating signature data from spatially distributed multiband sensors in order to attain maximal characterization of the targets of interest in a ballistic missile defense engagement.

Figure 2 shows some components that must be incorporated into a fusion-based central processor whose input is radar data from multiple sensors. Though several candidate processors could have been used for this study, this report focuses on image processing, which requires several ingredients for fusing data between multiple sensors: sensor coherence, a target-motion solution, and a suitable target model. Preprocessing the data to compensate for the various data-contamination effects that result from sensors that are spatially separated or operating over different frequency bands is necessary before an image can be generated. Once the data have been preprocessed, an image can be generated using either conventional image-processing algorithms (see Section 2) or enhanced data-fusion image processing that employs the sparse-band or sparse-angle processing techniques that are developed later in this report.

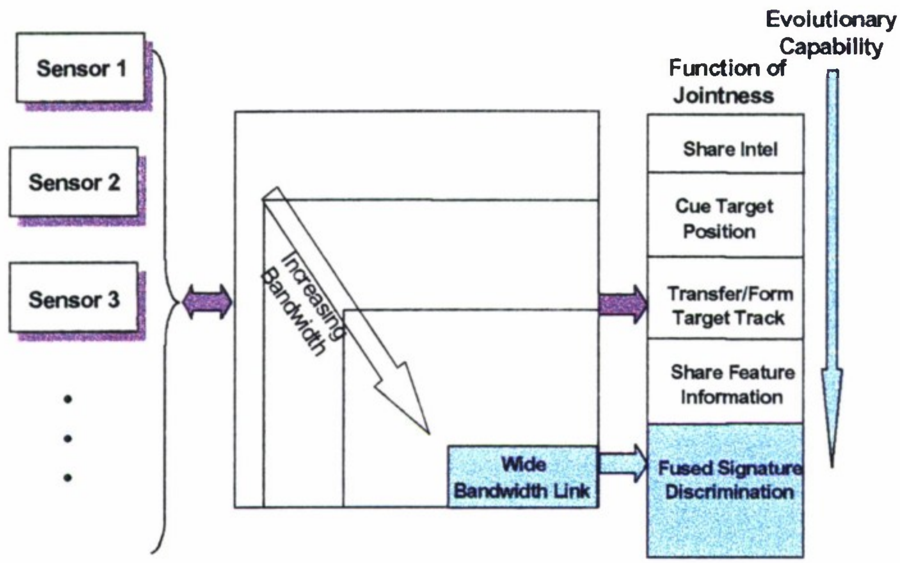

Figure 1. Family-of-systems elements.

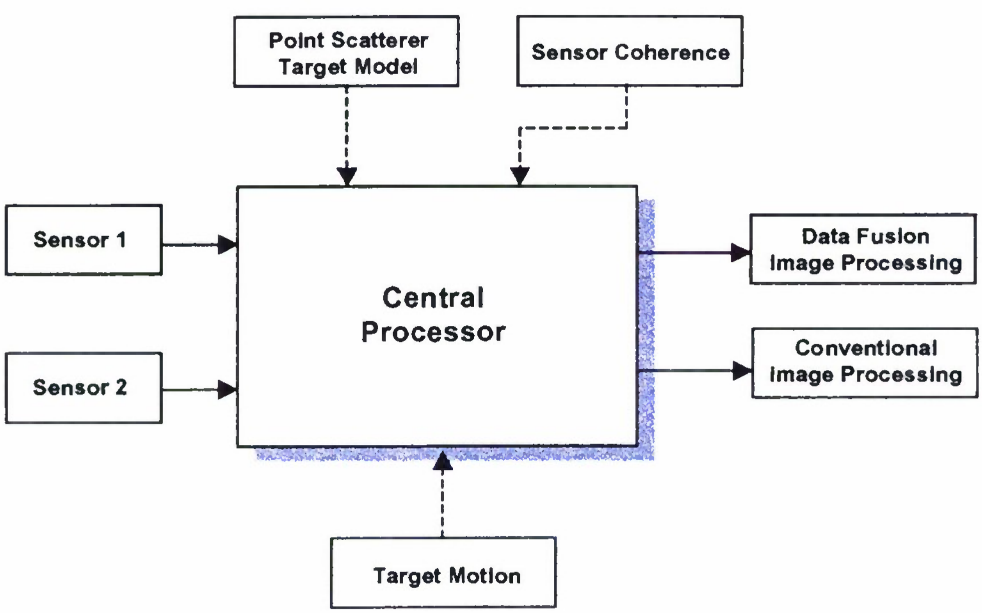

Figure 2. Model of central processor, showing inputs, possible components (dotted lines), and outputs.

Figure 3 illustrates a scenario in which two spatially separated radars are interrogating an unknown target. Sensors 1 and 2 are located at distances R_1 and R_2, respectively, from the target; in general, the sensors operate over different frequency bands. The examples in this report assume that both sensors have the target in track and that a motion estimate is available. Although the effects of an error in the motion estimate are not considered in this report, the motion estimate is a key ingredient in associating a sequence of temporal measurements for radars operating independently (perhaps at different pulse repetition frequencies) with corresponding look angles to the target. (Bistatic processing is also possible for sensors operating in the same or in overlapping bands; however, bistatic processing is not considered here.) Methods for mutually cohering and formatting the data will be presented, as sensor coherence and proper data formatting are essential before coherent combination of the data. Mutual-coherence errors occur because of range-estimation errors, hardware differences, or angle-bias errors.

This report studies how the final image is affected by adding or removing components from the generic image processor shown in Figure 2. The goal is to obtain the best-possible image from multisensor data, so that the resultant image can be fed into a target characterization process for full characterization.

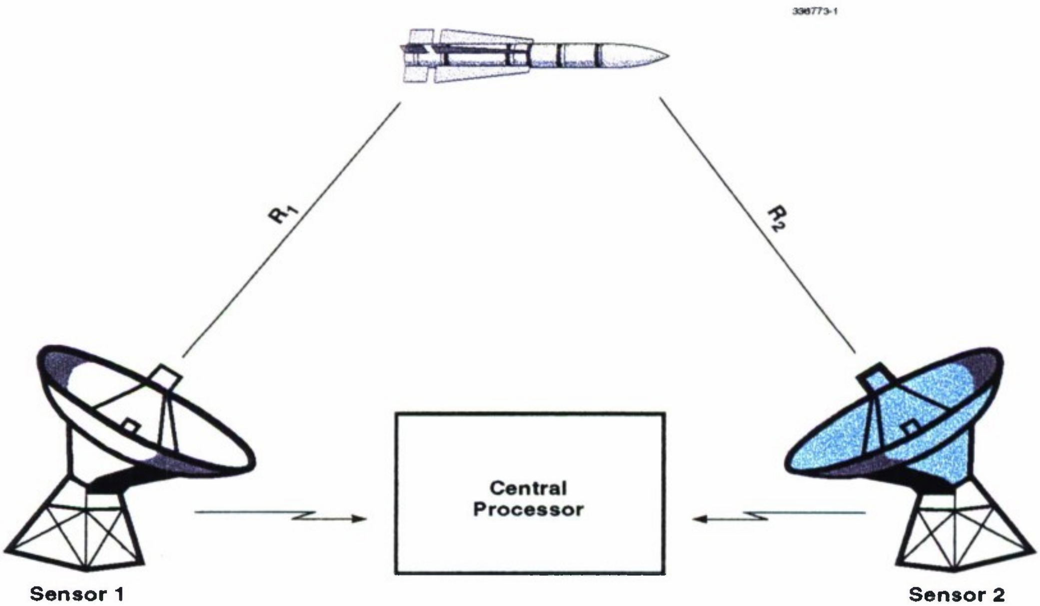

Figure 3. Two spatially separated sensors interrogating an unknown target.

2. CONCEPTS

2.1 DATA FORMATTING

This section reviews the methods that are commonly used to obtain focused images for continuous-wave and wideband signals. The review parallels the development of [2] and places the notation used in this report into a commonly accepted scheme. The review includes polar formatting of data, as this method will be used in a novel way within the context of ultrawide-bandwidth expansion for high-resolution imaging (see Section 4.1.2).

The two-dimensional geometry for analyzing radar return signals from an arbitrary target with a number of scattering centers at coordinates (x_m, y_m) is shown in Figure 4. The aspect angle, φ, is the angle between the x-axis and the radar line of sight (RLOS) vector; the target is assumed to be located at the center of this x-y coordinate system. As the target rotates, the RLOS vector sweeps through the target space, sampling a range of viewing angles of the object. The position of the RLOS vector is given by

$$R(\varphi) = \cos\varphi x + \sin\varphi y \quad , \tag{1}$$

where the vectors x and y denote unit vectors in the two-dimensional coordinate system.

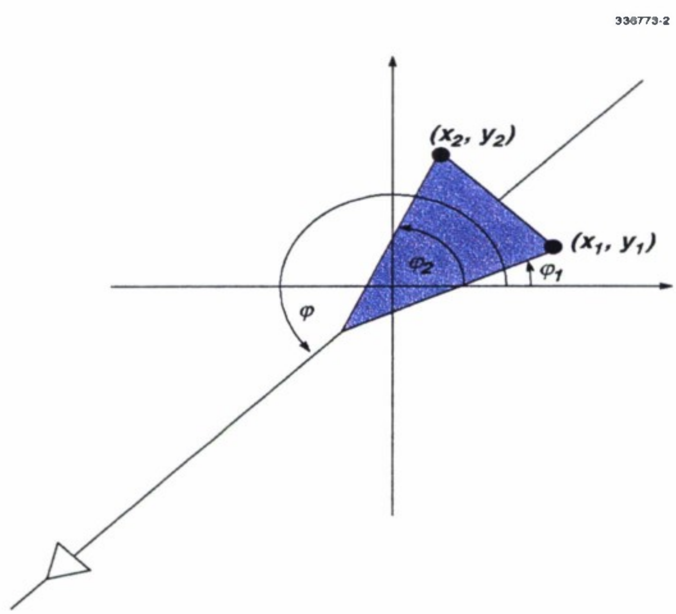

Figure 4. Two-dimensional geometry of target space.

The slant-range $R_m(\varphi)$ of the target point located at (x_m, y_m) is defined by projecting the target point onto the RLOS vector; i.e.,

$$R_m(\varphi) = x_m \cos\varphi + y_m \sin\varphi \quad . \tag{2}$$

This expression is of fundamental importance for radar signal processing: e.g., it tells that the slant-range history of any target point is a sinusoidal function of the target's rotation angle, φ. Now let the target be illuminated with a signal of the form $T(t) = e^{j\omega t}$. Assuming that the target consists of point sources located far from the radar, the received signal for each point source is given by

$$e_m(t) = \sigma_{c,m} e^{j\omega\left(t - \frac{2R_m(\varphi)}{c}\right)} \quad , \tag{3}$$

where the term $2R_m(\varphi)/c$ corresponds to the propagation delay between transmission of $T(t)$ and reception of $e_m(t)$, referred to a target-centered coordinate system. The constants c and σ_c denote the speed of propagation and the radar cross section of the point source, respectively, where σ_c is used for the complex cross section and is defined such that $\sigma = |\sigma_c|^2$. The baseband received signal for targets containing M pointlike scattering centers is obtained by demodulating the signal and coherently summing the responses from individual scatterers and is given by

$$e(t) = \sum_{m=1}^{M} e_m(t) e^{-j\omega t} = \sum_{m=1}^{M} \sigma_{c,m} e^{-j\omega \frac{2}{c} R_m(\varphi)} \quad . \tag{4}$$

When a target is scanned over a range of frequencies and viewing angles, Equation (4) may be interpreted in terms of a two-dimensional target function $E(f,\varphi)$, which can be written as

$$E(f,\varphi) = \sum_{m=1}^{M} \sigma_{c,m} e^{-j\frac{4\pi f}{c}(x_m \cos\varphi + y_m \sin\varphi)} \quad . \tag{5}$$

Equation (5) illustrates that the phase of the received signal varies as a function of radar look angle. These phase variations introduce focusing errors into an image by causing apparent motion of the objects through resolution cells; this motion in turn results in a smeared image for objects offset from the center of the image space. A focused image therefore requires that a phase correction be applied to every term of the sum for each angle φ and each point (x,y). This requirement leads to an image processor whose form is the conventional image integral:

$$I(x,y) = \int_{\varphi}\int_{f} E(f,\varphi) e^{j\frac{4\pi f}{c}(x \cos\varphi + y \sin\varphi)} \, df d\varphi \quad . \tag{6}$$

Though the image integral of Equation (6) is the correct operation for focused imaging, an image processor that could be expressed in the form of a Fourier transform integral would be more desirable for computational purposes. There are two methods that are commonly used to achieve this: small-angle approximations (linear imaging) and polar formatting.

2.1.1 Linear Imaging

Let Equation (6) be partitioned into a sum of integrals over small angular segments and frequency steps:

$$\begin{aligned} \varphi &= \varphi_k + \Delta\varphi \\ f &= f_0 + \Delta f \quad , \end{aligned} \tag{7}$$

where φ_k is the center of the segment, $\Delta\varphi$ are the angular steps about φ_k, f_0 is the center frequency, and Δf is the frequency step size. The integral of Equation (6) can now be written as

$$I(x,y) \approx \int_{\Delta\varphi}\int_{\Delta f} E(f_o + \Delta f, \varphi_k + \Delta\varphi) e^{j\frac{4\pi(f_o + \Delta f)}{c}(x\cos(\varphi_k + \Delta\varphi) + y\sin(\varphi_k + \Delta\varphi))} d\Delta f d\Delta\varphi \quad . \tag{8}$$

Using the identities

$$\begin{aligned} \cos(\varphi_k + \Delta\varphi) &= \cos\varphi_k \cos\Delta\varphi - \sin\varphi_k \sin\Delta\varphi \\ \sin(\varphi_k + \Delta\varphi) &= \sin\varphi_k \cos\Delta\varphi - \sin\Delta\varphi \sin\varphi_k \end{aligned}$$

and the relations

$$\begin{aligned} &\sin\Delta\varphi \cong \Delta\varphi \\ &\cos\Delta\varphi \cong 1 \\ &\Delta f \Delta\varphi \ll 1 \quad , \end{aligned}$$

Equation (8) becomes

$$I(x,y) \approx \sum_k e^{j\frac{4\pi f_o}{c}(x\cos\varphi_k + y\sin\varphi_k)} \times$$

$$\int_{\Delta\varphi}\int_{\Delta f} E(f_o + \Delta f, \varphi_k + \Delta\varphi) e^{j\frac{4\pi}{c}(x\cos\varphi_k + y\sin\varphi_k)\Delta f} e^{j\frac{4\pi f_o}{c}(-x\sin\varphi_k + y\cos\varphi_k)\Delta\varphi} d\Delta f d\Delta\varphi \quad . \tag{9}$$

Equation (9) is a two-dimensional Fourier transform on the $(\Delta f, \Delta\varphi)$ variables and can be solved efficiently using the discrete Fourier transform. The coefficient of the factor Δf in the exponent of Equation (9) represents the range to the m^{th} scatterer, and the coefficient of $\Delta\varphi$ represents the cross range of the m^{th} scatterer, relative to the center of the (x,y) system; hence, wide bandwidth produces improved range resolution, and wide angular coverage produces improved cross-range resolution.

It is instructive to observe what happens if an image is generated by processing $E(f,\varphi)$ in Equation (5) over large angular spans with a two-dimensional Fourier transform rather than the integral of Equation (6). An equivalent way of expressing $E(f,\varphi)$ is

$$E(f,\varphi) = \sum_m \sigma_m e^{-j\frac{4\pi f r_m}{c}\cos(\varphi - \varphi'_m)} \quad . \tag{10}$$

Figure 5 shows points in the (f,φ) plane where the phase of $E(f,\varphi)$ is constant and equal to multiples of 2π:

$$2\pi n = \frac{4\pi f r}{c}\cos(\varphi - \varphi') \quad . \tag{11}$$

Figure 5 plots Equation (11) for $n = 1, 5, 10, \ldots, 95, 99$, $0\ \mathrm{GHz} \le f \le 10\ \mathrm{GHz}$, $r = 1.5$, and $-\frac{\pi}{2} \le \varphi - \varphi' \le \frac{\pi}{2}$.

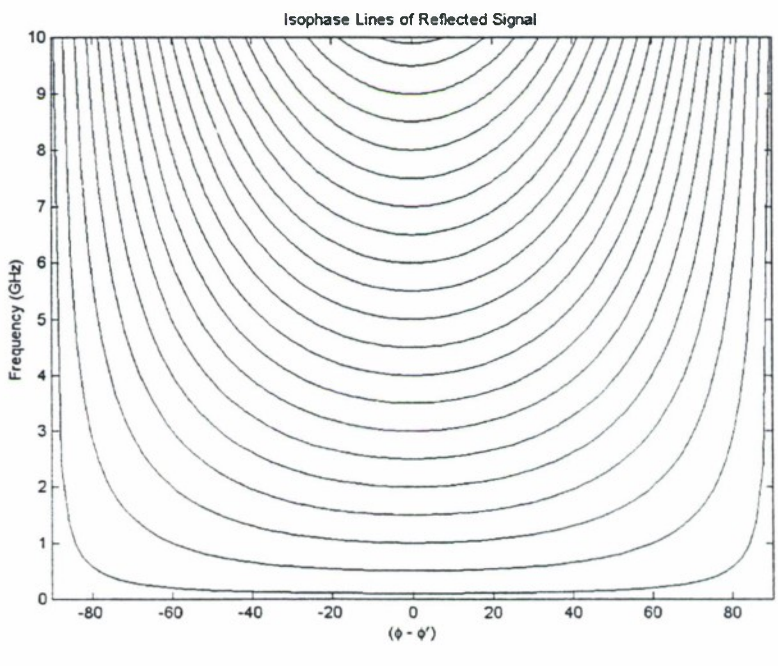

Figure 5. Isophase lines of reflected signal in (f,φ) space.

By differentiating Equation (11) with respect to f and φ, respectively,

$$\frac{\partial n}{\partial f} = \frac{2r}{c}\cos(\varphi - \varphi')$$
$$\frac{\partial n}{\partial \varphi} = \frac{-4\pi f r}{c}\sin(\varphi - \varphi') \quad . \tag{12}$$

Clearly a one-dimensional Fourier transform over f with constant φ will yield the correct range profile, as the spacing between isophase lines is constant along f for a given φ; however, a one-dimensional Fourier transform over φ with constant f will not yield the correct cross-range profile, as the spacing between isophase lines varies along φ for a given f. This variation in phase produces an unfocused image when $E(f,\varphi)$ is processed in a rectangular format using the two-dimensional Fourier transform. Figure 5 also provides insight as to why the small-angle approximation in Equation (9) produces a focused image: over limited regions of the (f,φ) plane the spacing between isophase lines is approximately equal in both f and φ.

2.1.2 Polar Formatting and Extended Coherent Processing

Polar formatting, the second Fourier-based method for producing focused images, maps the curved isophase lines of Figure 5 into straight, parallel lines that allow use of the two-dimensional Fourier transform with wide-angle data. The mapping of $E(f,\varphi) \rightarrow E(u,v)$ is accomplished as follows. Using the relations

$$u = \frac{4\pi f}{c}\cos\varphi$$
$$v = \frac{4\pi f}{c}\sin\varphi \quad , \tag{13}$$

the image integral of Equation (6) can be rewritten as

$$I(x,y) = \iint_{v\,u} E(u,v)e^{j(ux + vy)}du\,dv \quad , \tag{14}$$

where $E(u,v)$ is $E(f,\varphi)$ resampled in nonuniform increments of f and φ corresponding to uniform increments of u and v. Equation (14) is traditionally used to achieve wide-angle imaging beyond those angular sectors for which linear imaging is valid. Resampling can be done using any number of interpolation methods. The transformation of Equation (13) maps a rectangular region in (f,φ) space into an annular sector in (u,v) space, as shown in Figure 6.

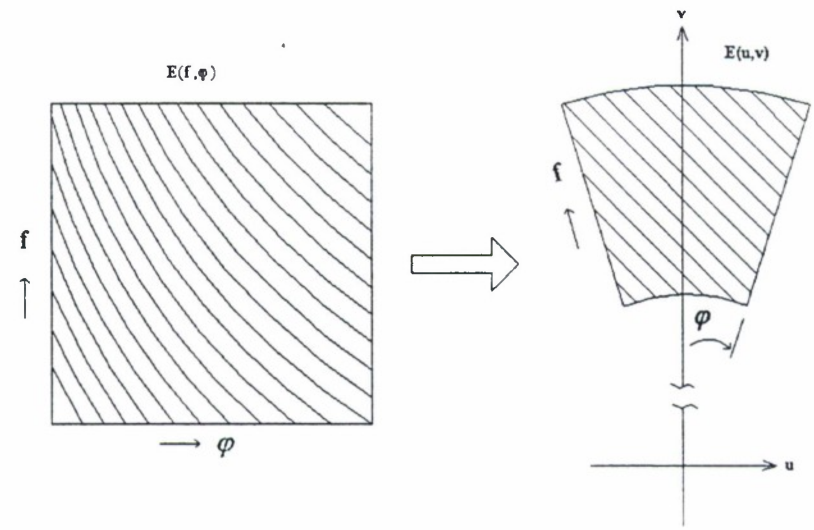

Figure 6. Mapping of rectangular region of (f,φ) *space to annular sector of* (u,v) *space.*

Figure 7 shows the isophase lines of Equation (14) plotted using

$$2\pi n = ux + vy \quad , \tag{15}$$

where $x = r\cos\varphi'$ and $y = r\sin\varphi'$. The curved lines of Figure 5 are now straight, and the parallel lines are rotated from the v-axis by the angle φ'. Once this transformation has been accomplished, a focused image can be generated by processing the array of polar-formatted data using a two-dimensional Fourier transform. For continuous-wave imaging, the two-dimensional Fourier transform of Equation (14) becomes a line integral along a circular arc of radius $(4\pi f_o)/c$ in (u,v) space.

2.2 RESAMPLING FOR POLAR FORMATTING

Any number of interpolation methods might be employed for resampling data onto a uniform rectangular grid in (u,v) space. One fast and accurate interpolation scheme is based on a bilinear interpolation; it is the method used in this work. Figure 8 shows measured data in (f,φ) space overlaid onto a rectangular grid in (u,v) space. The measurement regions in (f,φ) space have been chosen as they would appear for two sensors separated in frequency and in angle; the (u,v) grid is chosen to encompass the entire measurement region. The goal is to extrapolate the data over the measurement region to this much-larger space, providing an image with increased sharpness and enhanced resolution.

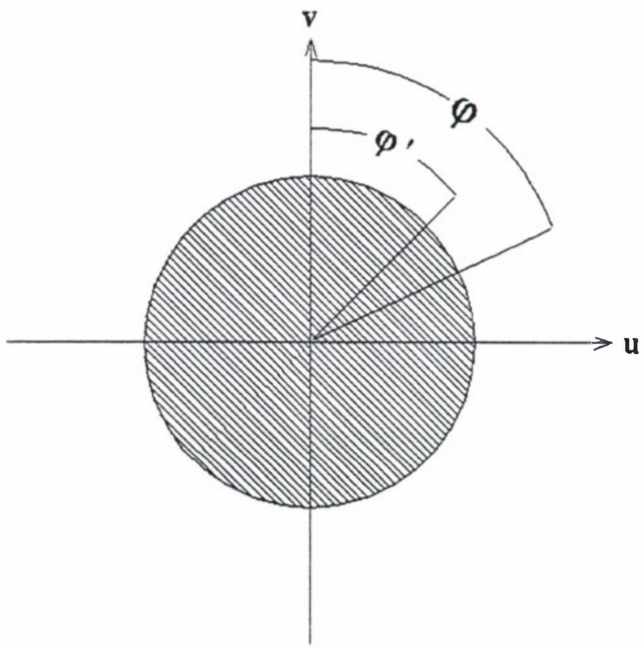

Figure 7. Isophase lines of reflected signal in (u,v) *space.*

To find any of the desired points in (u,v) space, use the four nearest neighbors in (f,φ) space to construct a system of equations given by

$$\begin{aligned} a_1 f_1 + a_2\varphi_1 + a_3 f_1\varphi_1 + a_4 &= E(f_1,\varphi_1) \\ a_1 f_2 + a_2\varphi_2 + a_3 f_2\varphi_2 + a_4 &= E(f_2,\varphi_2) \\ a_1 f_3 + a_2\varphi_3 + a_3 f_3\varphi_3 + a_4 &= E(f_3,\varphi_3) \\ a_1 f_4 + a_2\varphi_4 + a_3 f_4\varphi_4 + a_4 &= E(f_4,\varphi_4) \quad , \end{aligned} \tag{16}$$

which can be rewritten in matrix form as

$$\begin{bmatrix} f_1 & \varphi_1 & f_1\varphi_1 & 1 \\ f_2 & \varphi_2 & f_2\varphi_2 & 1 \\ f_3 & \varphi_3 & f_3\varphi_3 & 1 \\ f_4 & \varphi_4 & f_4\varphi_4 & 1 \end{bmatrix} \begin{bmatrix} a_1 \\ a_2 \\ a_3 \\ a_4 \end{bmatrix} = \begin{bmatrix} E(f_1,\varphi_1) \\ E(f_2,\varphi_2) \\ E(f_3,\varphi_3) \\ E(f_4,\varphi_4) \end{bmatrix} \quad . \tag{17}$$

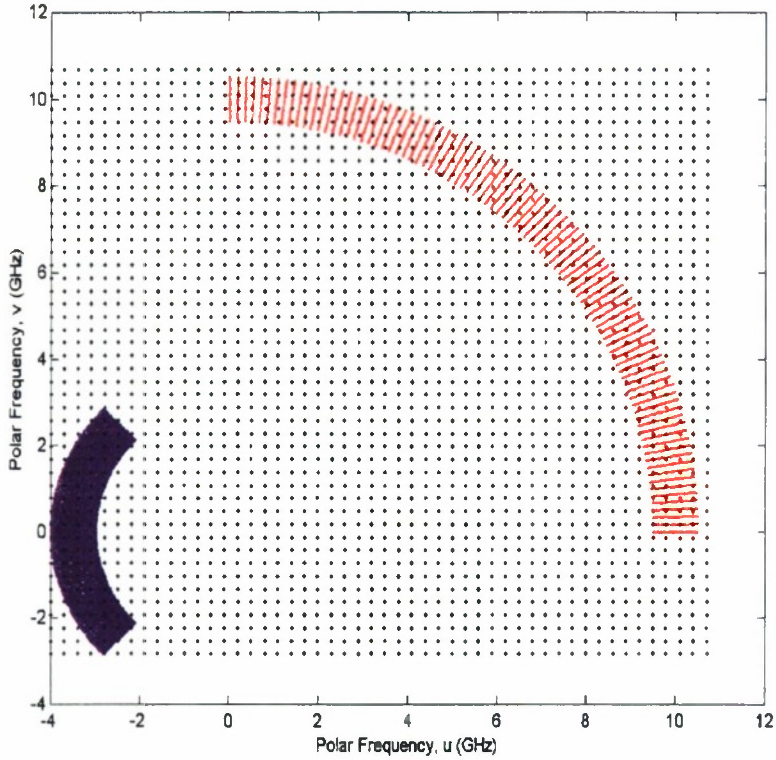

Figure 8. Data points in (f,φ) *space overlaid on a rectangular grid in* (u,v) *space.*

Figure 9 is a magnification of Figure 8 and shows more clearly the measured data points in (f,φ) space that are nearest neighbors to the desired data point in (u,v) space. Using Equation (17), determining coefficients $a_1, \ldots, a_4$ is straightforward. Once $a_1, \ldots, a_4$ are known, the desired point in (u,v) space can be found whose four nearest neighbors were used in Equation (16) and Equation (17).

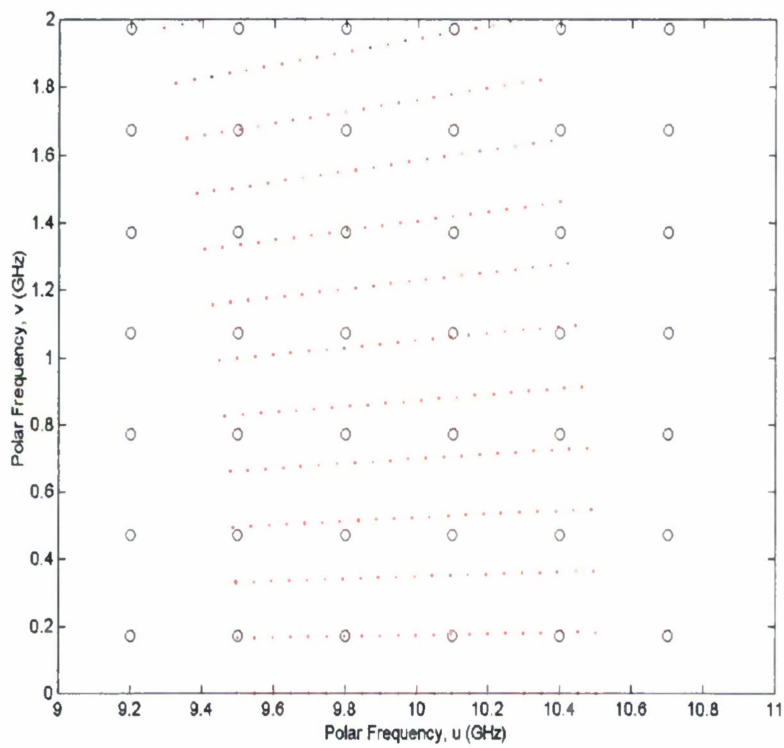

Figure 9. Magnification of Figure 8, showing nearest neighbors (dots) to desired data points (circles).

2.3 MODAL EXPANSION AND POLES IN (f,φ) SPACE

The utility of using the two-dimensional Fourier-transform–based method defined by Equation (14) for image processing becomes clear by rewriting Equation (5) in terms of the (u,v) variables:

$$E(f,\varphi) = \sum_{m=1}^{M} \sigma_{c,m} e^{-jux_m} e^{-jvy_m} \quad . \tag{18}$$

Thus a constant-amplitude point source located at (x_m,y_m) appears as a pure sinusoid in (u,v) space. This property is exploited further in Section 4.1 to develop an ultrawide-bandwidth fusion algorithm based on two-dimensional pole spectral-estimation techniques for ideal pointlike scatterers. This section uses a commonly-known modal expansion to contrast this (u,v) space simplicity to (f,φ) space processing.

The modal technique described here represents a signal in (f,φ) space as a sum of two-dimensional radiation modes given by

$$E(f,\varphi) = \sum_{n=-\infty}^{+\infty} D_n(f) e^{jn\varphi} \quad . \tag{19}$$

Motivation for using the modal representation of Equation (19) comes by expanding the exponential of Equation (10) into an infinite sum of cylindrical-wave functions of the form

$$e^{-j\frac{4\pi f r_m}{c}\cos(\varphi - \varphi'_m)} = \sum_{n=-\infty}^{+\infty} j^{-n} J_n\left(\frac{4\pi f r_m}{c}\right) e^{jn(\varphi - \varphi'_m)} \quad , \tag{20}$$

which allows the two-dimensional target function of Equation (10) to be written as

$$\begin{aligned} E(f,\varphi) &= \sum_m \sigma_m \sum_{n=-\infty}^{+\infty} j^{-n} J_n\left(\frac{4\pi f r_m}{c}\right) e^{jn(\varphi - \varphi'_m)} \\ &= \sum_{n=-\infty}^{+\infty} \underbrace{\left\{ \sum_m \sigma_m j^{-n} J_n\left(\frac{4\pi f r_m}{c}\right) e^{-jn\varphi'_m} \right\}}_{D_n(f)} e^{jn\varphi} \quad . \end{aligned} \tag{21}$$

As indicated in Equation (21), the mode coefficients $D_n(f)$ are defined by the bracketed term. If the mode coefficients $D_n(f)$ could be estimated from known data measured over a sparsely populated angular domain, Equation (21) could be used to extrapolate the signal $\hat{E}(f_0,\varphi)$ for the entire interval $0 \text{ deg} \le \varphi \le 360 \text{ deg}$; both range and cross-range resolution could then be improved by estimating the target signature over a full 360-deg rotation.

Consider now the special case where the argument of the Bessel function in Equation (22) is large (as in high-frequency applications where all-pole modeling techniques are valid; i.e., $4\pi f r_m / c \gg 1$), where the large-argument expansion of the Bessel function can be used:

$$\begin{aligned} J_n(x) &\approx \sqrt{\frac{2}{\pi x}} \cos\left(x - \frac{n\pi}{2} - \frac{\pi}{4}\right) \\ &= \sqrt{\frac{1}{2\pi x}} \left(e^{j\left(x - \frac{n\pi}{2} - \frac{\pi}{4}\right)} + e^{-j\left(x - \frac{n\pi}{2} - \frac{\pi}{4}\right)} \right) \quad . \end{aligned} \tag{22}$$

Substituting Equation (22) into Equation (21) and truncating the infinite summation to an appropriate number of terms gives

$$E(f,\varphi) = \sum_{n=-N}^{N} \left\{ \sum_{m} \sigma_m j^{-n} e^{-jn\varphi'_m} \sqrt{\frac{c}{8\pi^2 f r'_m}} \times \right.$$

$$\left. \left[e^{j\frac{4\pi f r'_m}{c}} e^{-j\frac{n\pi}{2}} e^{-j\frac{\pi}{4}} + e^{-j\frac{4\pi f r'_m}{c}} e^{+j\frac{n\pi}{2}} e^{+j\frac{\pi}{4}} \right] \right\} e^{jn\varphi} \quad , \qquad (23)$$

where $N \approx (4\pi f|r'_m|_{\max})/c$. Equation (23) shows that in the angle domain, $4N + 1$ pole combinations are generally required to represent each physical scatterer when viewed over the entire interval $0 \text{ deg} \leq \varphi \leq 360 \text{ deg}$. As $N \approx (4\pi f|r'_m|_{\max})/c$ can be quite large for high frequencies, there is motivation for the study of alternatives to all-pole modeling in the angle domain. For example, a 1-m target at X-band produces $N \approx 420$, so that roughly 1680 poles are required to characterize each scatterer over the entire interval!

2.4 MULTISENSOR FUSION: BASELINE PROCESSOR

Once the data from each sensor have been preprocessed for mutual coherence and transformed into a polar format, they might be combined using an image integral that is the coherent sum of subband subsector image integrals calculated from the output of each of N sensors, given by

$$\int_{v}\int_{u} E(u,v) e^{j(ux+vy)} du dv = \int_{v_1}\int_{u_1} E(u_1,v_1) e^{j(u_1 x + v_1 y)} du_1 dv_1$$
$$+ \int_{v_2}\int_{u_2} E(u_2,v_2) e^{j(u_2 x + v_2 y)} du_2 dv_2 + \ldots + \int_{v_N}\int_{u_N} E(u_N,v_N) e^{j(u_N x + v_N y)} du_N dv_N \quad . \qquad (24)$$

Equation (24) is a candidate method for fusing multisensor data, and it is used here as a baseline in comparing other candidate imaging techniques. Before data from multiple sensors can be used in Equation (24), the problem of sensor mutual coherence must be addressed; this problem is considered in the following section.

3. MUTUAL COHERENCE OF MULTISENSOR DATA

3.1 GENERAL FORMULATION VS. RANGE/ANGLE BIAS

Mutual-coherence problems occur when data are collected independently by spatially separated sparse-band sensors. It is convenient to partition this separation into two categories: range separation and angle separation. Range-only coherence errors result when two or more sensors interrogate a target at the same look angle but there is an error ΔR between range estimates for each sensor. For this case the target is in the far field of two nearly collocated sensors and the far-field criterion $2D^2/\lambda$ is met, where D is the separation distance between sensors projected perpendicular to the RLOS to the target. Angle-coherence errors arise when this far-field criterion is not met, so that the target is in the near field (when interpreting the sensors as having a separation aperture of distance D) and there is an error in angle $\Delta\varphi$ in each sensor's look angle to the target.

To examine the effects of range- and angle-coherence errors, consider the two-sensor geometry illustrated in Figure 10. Two sensors are assumed to operate independently, interrogate the target at angles φ_1 and φ_2, respectively, and have bandwidths BW_1 centered at f_1 and BW_2 centered at f_2. The target is assumed to be in motion, which is determined by two basic components: a ballistic motion $\bar{V}_0$, generally characterized by the motion of the center of gravity of the target, and a localized motion $\bar{V}_n$ about the center of rotation of the body. This latter motion leads to short time interval range-Doppler images of the target caused by the motion $\bar{V}_n$, which is the focus of this report. This phenomenology is to be contrasted with longer-time inverse synthetic aperture radar (ISAR) imaging, where changes in look angle to the target are obtained from changes in $\bar{V}_0$.

The baseband received waveforms, before pulse compression, are given by

$$E_1(\omega,\varphi_1) = |T_1(\omega)|^2 F_1^2(\omega+\omega_1,\varphi_1)e^{-j2\left(\frac{\omega+\omega_1}{c}\right)R_1} \times \sigma_c(\omega+\omega_1,\varphi_1)e^{j\psi_1}e^{-j\omega\tau_1}$$

$$-\frac{BW_1}{2} \le f \le \frac{BW_1}{2} \quad , \qquad (25)$$

$$E_2(\omega',\varphi_2) = |T_2(\omega')|^2 F_2^2(\omega'+\omega_2,\varphi_2)e^{-j2\left(\frac{\omega'+\omega_2}{c}\right)R_2} \times \sigma_c(\omega'+\omega_2,\varphi_2)e^{j\omega'_2}e^{-j\psi\tau_2}$$

$$-\frac{BW_2}{2} \le f \le \frac{BW_2}{2} \quad , \qquad (26)$$

where R_1 and R_2 denote the ranges to the target for sensors 1 and 2, respectively. $T_1(\omega)$ and $T_2(\omega')$ are the baseband transmitted waveforms, where

$$-\frac{BW_1}{2} \le f \le \frac{BW_1}{2} \qquad (27)$$

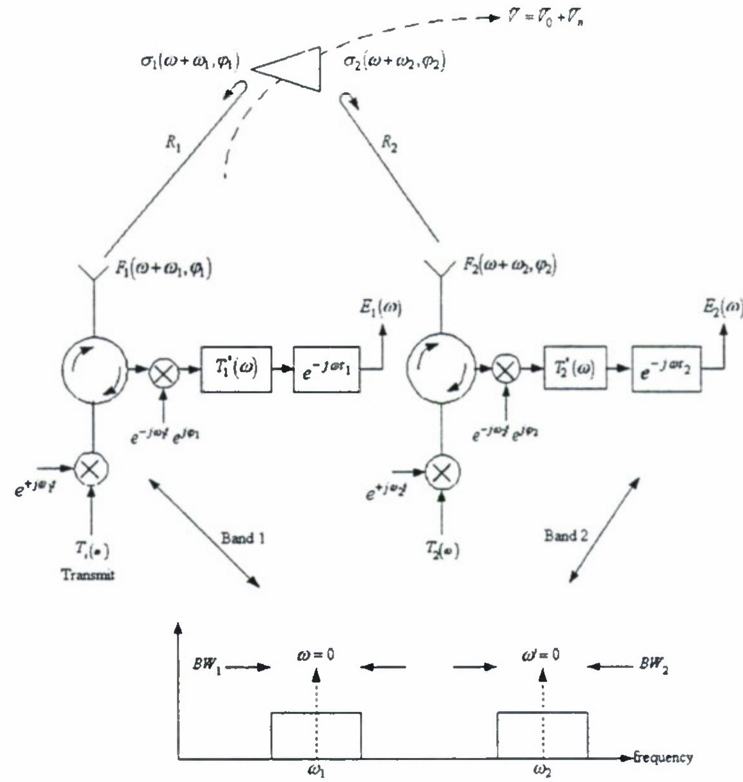

Figure 10. Geometry for two-sensor mutual-coherence characterization.

and

$$-\frac{BW_2}{2} \leq f' \leq \frac{BW_2}{2} \quad , \tag{28}$$

and $\omega = 2\pi f$, $\omega' = 2\pi f'$. $F_1(\omega)$ and $F_2(\omega')$ denote the antenna frequency-response functions, and $\sigma_c(\omega,\varphi)$ represents the target's complex radar cross section (introduced in Section 1), which is a function of both angle and frequency. Allowance is made for phase and delay offsets (ψ_1,τ_1) and (ψ_2,τ_2) for each sensor, which result from hardware differences between sensors.

Because the objective is to fuse multisensor signature data over a given time interval, a number of pulses will be processed. For a conventional wideband radar, R and φ are essentially constant over a single processing pulse of length T; thus, changes in R_1, R_2, φ_1, and φ_2 are considered only over pulse increments on Δt, where Δt denotes the pulse repetition interval. Thus

$$\left.\begin{aligned} R_1(n) &= R_{10} + V_1 n\Delta t \\ R_2(n) &= R_{20} + V_2 n\Delta t \\ \varphi_{1,n} &= \varphi_{10} + n\Delta\varphi_1 \\ \varphi_{2,n} &= \varphi_{20} + n\Delta\varphi_2 \end{aligned}\right\} n = 0,\, 1,\, \ldots \quad . \tag{29}$$

For each sensor the response function $|T(\omega)|^2 F^2(\omega + \omega_{1,2})$ is generally known and is equalized by calibration, so this term is omitted from each response. $E_1(\omega)$ and $E_2(\omega')$ can then be expressed in the form

$$E_1(\omega,n) = \sigma_c(\omega + \omega_1, \varphi_{1,n}) \times \left\{ e^{j\Psi_1} e^{-j\omega\tau_1} e^{-j\frac{2\omega}{c}R_1(n)} e^{-j\frac{2\omega_1}{c}R_1(n)} \right\} ,$$

$$E_2(\omega',n) = \sigma_c(\omega' + \omega_2, \varphi_{2,n}) \times \left\{ e^{j\Psi_2} e^{-j\omega\tau_2} e^{-j\frac{2\omega'}{c}R_2(n)} e^{-j\frac{2\omega_2}{c}R_2(n)} \right\} , \tag{30}$$

where $R_1(n)$, $R_2(n)$, $\varphi_{1,n}$, and $\varphi_{2,n}$ are given by Equation (29).

Equation (30) forms the basis for linking the data collected by each sensor. Equation (30) is divided into two parts: to the left of the multiplication symbol is indicated the ideal response associated with $E_1(\omega,n)$ and $E_2(\omega',n)$; i.e., the complex radar cross section of the target. The cross section σ_c is unique to the target only and is analogous to what would be measured on an error-free radar cross section range. The quantities within the brackets to the right of the multiplication symbol denote corrections required in the data that would corrupt coherent multisensor data fusion: these errors must be removed from the data before sensor fusion can take place. In practice, the required phase correction represents the most formidable problem. Each of these factors is now addressed separately.

3.1.1 Phase-Shift Offset and Hardware Time Delay

The phase-shift offset $e^{j\psi_1}$ is similar to that considered in [1]; it represents a combination of hardware and range-propagation phase errors. Generally the procedure is to reference one sensor to another, representing a phase shift $e^{j(\psi_2 - \psi_1)}$ that must be removed from the data. The hardware time delay is similar in form to the range-delay factor and will be considered in Section 3.1.3.

3.1.2 Range-Rate Compensation and Pulse Alignment

The pulse-to-pulse change of the range line-of-sight from each sensor to the target is characterized by the last factor on the right-hand side of Equation (30). Typically these terms are removed from the data by the process of pulse alignment, in which differences in range caused by $\Delta R(n) = Vn\Delta t$ are corrected. A smoothed state vector $\hat{R}(t)$ characterizing the range to the target's center of gravity is developed by the range tracker over many pulses of processed data. Each pulse is then aligned to $\hat{R}(t)$, with data compensation given by

$$e^{+j\frac{4\pi V}{\lambda}n\Delta t} ,$$

where $\Delta R = Vn\Delta t$ and $\lambda = \lambda_1$ or $\lambda = \lambda_2$, as appropriate for each sensor. Compensation for the phase offset induced by this term can be combined into the phase term discussed in Section 3.1.1.

3.1.3 Frequency-Dependent Range Effects

The middle factor on the right-hand side of Equation (30) causes a frequency-dependent distortion. The effect of this term for a given pulse is to offset the position of the wideband received pulse, resulting in an error in range estimate to the target. Typically this term is removed by appropriately setting the receive sampling gates according to the position determined by the range-tracker estimate $\hat{R}(t)$. Error biases $R_{1,B}$ and $R_{2,B}$ for each respective sensor relative to $\hat{R}(t)$ cause a shift in the position of the processed wideband pulse. For a single sensor this shift in absolute position is generally unimportant for wideband radar imaging; however, it must be compensated for when processing data from multiple sensors.

3.2 MUTUAL-COHERENCE COMPENSATION

The above development forms the basis for determining the compensation that must be applied to multisensor data in order to fuse multisensor signature data over different look angles and frequency bands. The net effect of the various compensation mechanisms required can be partitioned into the error sources delineated in Table 1.

TABLE 1
Error Sources and Mutual-Coherence Effects

Error Source	Mutual-Coherence Effect
Hardware/Propagation Phase Offets	$e^{j\psi}$
Hardware Delays	$e^{-j\omega\tau_o}$
Range-Bias Estimation Errors	$e^{-j\omega(\Delta R/c)}$
Angle-Bias Estimation Errors	
• Angle Bias	$\varphi \rightarrow \varphi + \Delta\varphi_B$
• Motion → Angle	$\varphi \rightarrow \varphi + \Delta\varphi(t)$

The effect of these errors is to cause an error in the estimation of the complex radar cross section $\sigma_c(f,\varphi)$ of the target. This effect can be succinctly summarized for two sensors by referencing the error sources to the first sensor. Denote by $E_1(f,\varphi)$ and $E_2(f,\varphi)$ the estimates of σ_c over sectors Ω_1 and Ω_2 (the sector observation angles of sensors 1 and 2 relative to φ_1 and φ_2) and bandwidths BW_1 and BW_2, respectively:

$$E_1(f,\varphi) \approx \sigma_c(f_1 + f, \varphi_1 + \varphi) \quad , \begin{cases} |f| \le BW_1 \\ |\varphi| \le \Omega_1 \end{cases} \quad ,$$

$$E_2(f,\varphi) \approx \sigma_c(f_2 + f, \varphi_2 + \Delta\varphi_B + \varphi) e^{j\psi} e^{-j\omega\tau} \quad , \begin{cases} |f| \le BW_2 \\ |\varphi| \le \Omega_2 \\ \tau = \Delta\tau + 2\Delta R/c \end{cases} \quad , \tag{31}$$

where the system (hardware) delay and range-bias delay errors are combined into the common term

$$\tau \equiv \tau_2 - \tau_1 + 2(R_{2,B} - R_{1,B})/c \quad . \tag{32}$$

The notation of a common baseband frequency variable f versus ω and ω' is the same here as was used previously.

Examination of Equation (31) reveals that coherent processing of multisensor data requires compensation for range delay, aspect-angle estimation errors, and constant-phase effects. Two special cases that deserve special consideration are discussed in the following subsections.

3.2.1 Common Look Angle, Different Frequency Bands

For common look angle and different frequency bands, the phase offset ψ and delay error τ must be compensated for in the data from band 2 according to $e^{-j\psi} e^{+j\omega\tau}$ before data fusion. Techniques for estimating τ and compensating the data in band 2 are developed in [1].

3.2.2 Different Look Angles, Narrow Bandwidth

For narrow bandwidths the frequency-dependent delay error $e^{-j\omega\tau}$ reduces to a phase-offset error, and the angle-bias error dominates. As discussed in Section 2.1, it is assumed in this report that an accurate motion solution is available; thus, errors in $\Delta\varphi(t)$ caused by an inaccurate motion solution are outside the scope of the report.

To compensate for angle-bias errors between sensors, cross-section data $\sigma_c(\varphi_2 + \varphi + \Delta\varphi_B)$ must be shifted in angle by $\Delta\varphi_B$ before coherent combination with $\sigma_c(\varphi_1 + \varphi)$. A technique is now developed for estimating and compensating for $\Delta\varphi_B$; the technique is analogous to the pole-rotation compensation technique developed in [1] for delay compensation. In effect, differences in delay error $(\tau_2 - \tau_1)$ cause a range misalignment that manifests itself as a pole offset. The difference $\Delta\varphi_B$ causes a cross-range misalignment and results in a similar pole-offset effect.

Consider a simple two-point scatterer model example, as illustrated in Figure 11. The angular variation of $E(\varphi)$ at center frequency $f = f_1$ is given by

$$E(\varphi) = D_1 + D_2 e^{j\frac{4\pi f_1}{c} a\cos\varphi} \quad . \tag{33}$$

The poles associated with this simple two-point scatterer model over the region $\varphi_1 + \Omega_1$ can be determined using the expansion $\varphi = \varphi_1 + n\Delta\varphi$, where $\Delta\varphi$ denotes a small angular increment and $n = 0, 1, \ldots, N$. Using the angle-sum formula for $\cos(\varphi_1 + n\Delta\varphi)$ and assuming $n\Delta\varphi \ll 1$, $E(\varphi_1 + n\Delta\varphi)$ can be written in the form

$$E_n = D_1 + D_2 e^{j\frac{4\pi f_1}{c} a\cos\varphi_1} e^{-j\frac{4\pi f_1}{c} a\sin\varphi_1 (n\Delta\varphi)} \quad . \tag{34}$$

Rewriting the sequence $\{E_n\}$ in the form

$$E_n = D_1 + D_2 e^{j\frac{4\pi f_1}{c} a\cos\varphi_1} \left[e^{-j\frac{4\pi f_1}{c} a\Delta\varphi\sin\varphi_1} \right]^n \tag{35}$$

identifies two complex poles corresponding to each of the two scatterers. These are located on the unit circle and are displaced in angle by

$$\alpha_1 = -\frac{4\pi f_1}{c} a\Delta\varphi\sin\varphi_1 = -\frac{4\pi f_1}{c} \rho_{CR}\Delta\varphi \quad , \tag{36}$$

where the cross range is defined as $\rho_{CR} = a\sin\varphi_1$. Thus a cross-range image at the angle φ_1 would appear as in Figure 12, as compared with a cross-range image at corresponding angle φ_2. The associated pole plot is illustrated in Figure 13.

A second sensor located at $\varphi = \varphi_2$ would measure two poles displaced in angle by Equation (36), with φ_1 replaced by φ_2. Consider now the positioning of the poles for two cases: for $\varphi = \varphi_2$ and for a bias error $\varphi = \varphi_2 + \Delta\varphi_B$. Assume $\varphi_2 > \varphi_1$, for which $\sin\varphi_2 > \sin\varphi_1$. For $\varphi = \varphi_2$, the cross range is given by $a\sin\varphi_2$, and the cross-range image is as indicated in Figure 12 for $\varphi = \varphi_2$. The cross-range image lines for $\varphi = \varphi_1$ and $\varphi = \varphi_2$ intersect at the scatterer location, so the two cross-range images can be combined coherently to infer the true scatterer locations to within an ambiguity of two other intersecting points. The corresponding pole locations for $\varphi = \varphi_2$ are shown on the unit circle of Figure 13; however, if the estimate of φ_2 is incorrect, i.e., if it is assumed

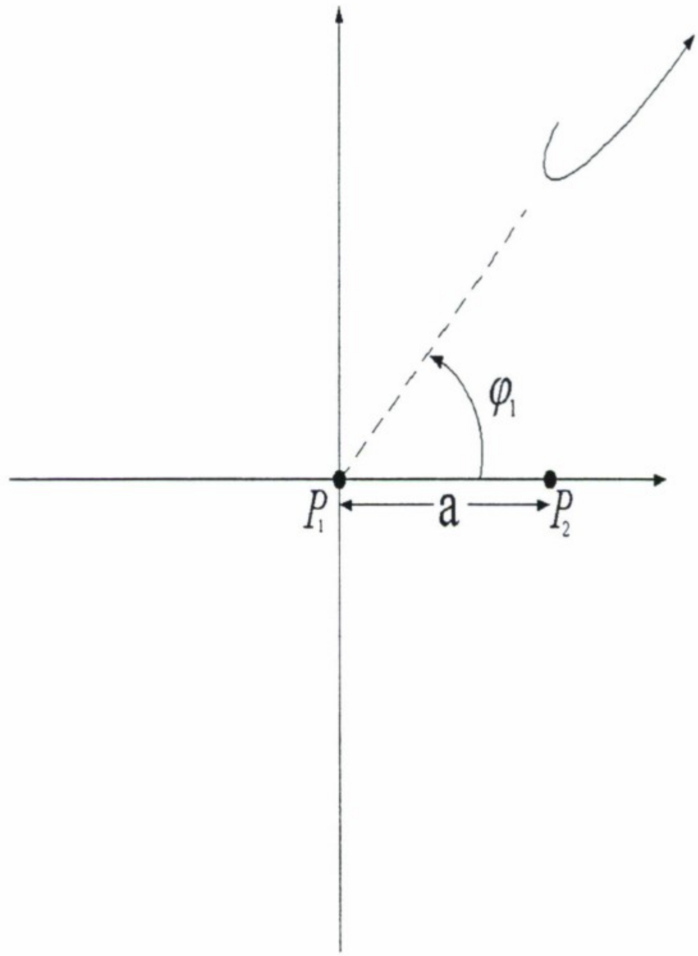

Figure 11. Two-point scatterer model example.

$$\hat{\varphi}_2 = \varphi_2 + \Delta\varphi_B \quad , \tag{37}$$

the cross-range image for $\hat{\varphi}_2 = \varphi_2 + \Delta\varphi_B$ would appear as the dashed image in Figure 12. The resulting intersection of the two cross-range images leads to an error in estimating the position of the scatterers, and the location of the pole $P_2(\varphi = \varphi_2)$ has been displaced to $P_2(\varphi = \varphi_2 + \Delta\varphi_B)$.

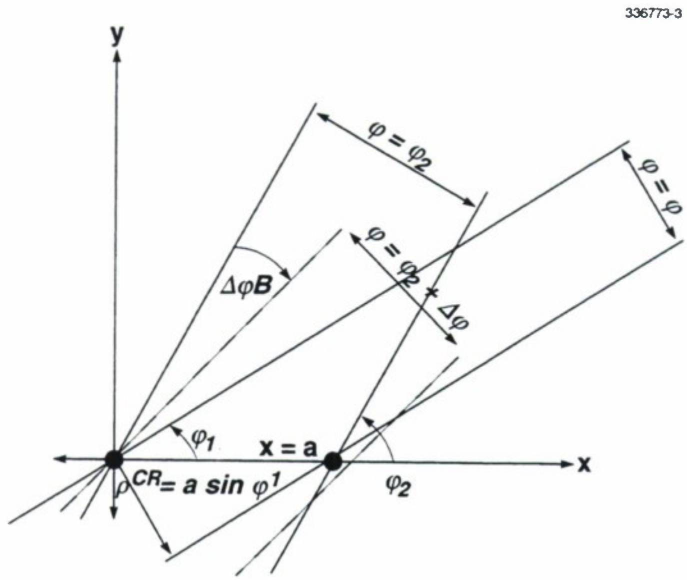

Figure 12. Cross-range image.

The process of determining $\Delta\varphi_B$ from the pole plot is straightforward. The spectral estimate for the cross range at either angle produces the correct result; the association of ρ_{CR_2} with the incorrect estimate $\hat{\varphi}_2$ is in error. Thus

$$\frac{\sin\varphi_2}{\sin\varphi_1} = \frac{\rho_{CR_2}}{\rho_{CR_1}} \quad , \tag{38}$$

so that

$$\varphi_2 = \sin^{-1}\sin\varphi_1\frac{\rho_{CR_2}}{\rho_{CR_1}} \quad , \tag{39}$$

and the bias error $\Delta\varphi_B$ is given by

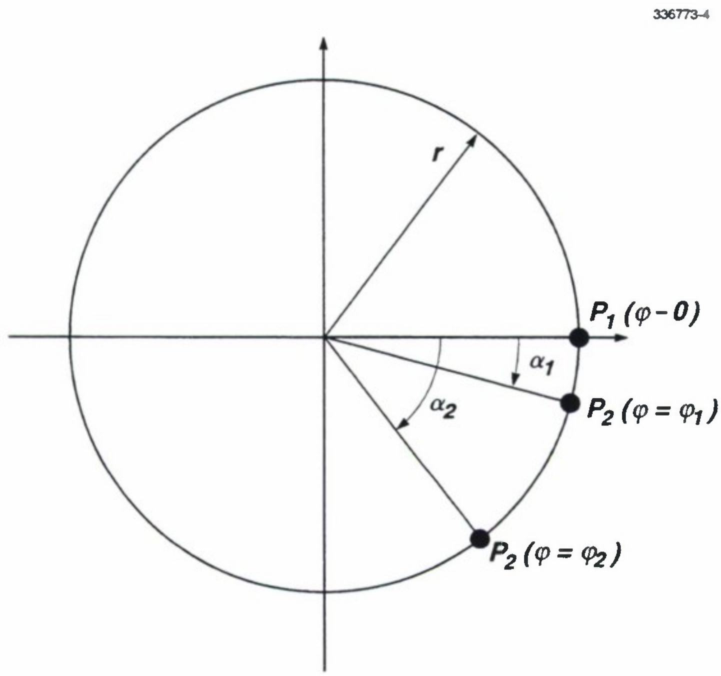

Figure 13. Cross-range poles for two-point scatterer.

$$\Delta\varphi_B = \hat{\varphi}_2 - \sin^{-1}\left(\sin\varphi_1 \frac{\rho_{CR_2}}{\rho_{CR_1}}\right) \quad . \tag{40}$$

Using $\Delta\varphi_B$ to correct the image alignment in Figure 12 will produce the correct source location.

Equation (40) can be interpreted as a pole-rotation correction. The pole that occurs at $P_2(\varphi = \hat{\varphi}_2)$ is the correct pole position; i.e., the cross-range separation predicted by the pole positions is indeed true. The right-hand term in Equation (40) rotates pole $P_2(\varphi = \hat{\varphi}_2)$ into P_1, determines the proper angle φ_2, and corrects the angle estimate $\hat{\varphi}_2$.

3.3 RANGE BIAS AND ANGLE BIAS MUTUAL-COHERENCE DUALITY

The coherence duality between the range-bias problem and the angle-bias problem is striking. This duality is summarized in Figure 14, which illustrates the coherence compensation duality between sparse-band frequency processing and sparse-sector angle processing.

Range-bias errors lead to an offset of the wideband pulse processed by each sensor. If these pulses are combined without compensating for the range-bias error, the relative position of the scatterers indicated by the wideband compressed pulse do not match, resulting in misidentification of the number of scattering centers. The locations of these scatterers for each subband are characterized by (1) a pole plot for each subband spectral estimate, and (2) the pole-rotation angle, which causes the subband pole estimates to coalesce into one estimate that characterizes the delay and range-bias errors. Analogously, for narrowband sensors with different look angles to the target, processing each subsector leads to a cross-range profile of the target. If these cross-range profiles are lined up without angle-bias compensation, common scattering points do not coincide, and once again misidentification of scattering centers occurs.

Generalization of this discussion to two wideband sensors located at different angular positions is simple. Each sensor is able to form an image of the target, with image quality dependent on subbandwidth (range resolution) and angular sector size (cross-range resolution). Proper multisensor fusion allows coherent combination of these images for improved image quality. Range- and system-delay mismatches between sensors result in a range misalignment for each image, angle-bias errors result in a cross-range misalignment, and phase errors result in less coherent processing gain in combining corresponding image points. Coherent signature fusion can be accomplished only when the sensors are mutually cohered to eliminate these misalignments and phase errors.

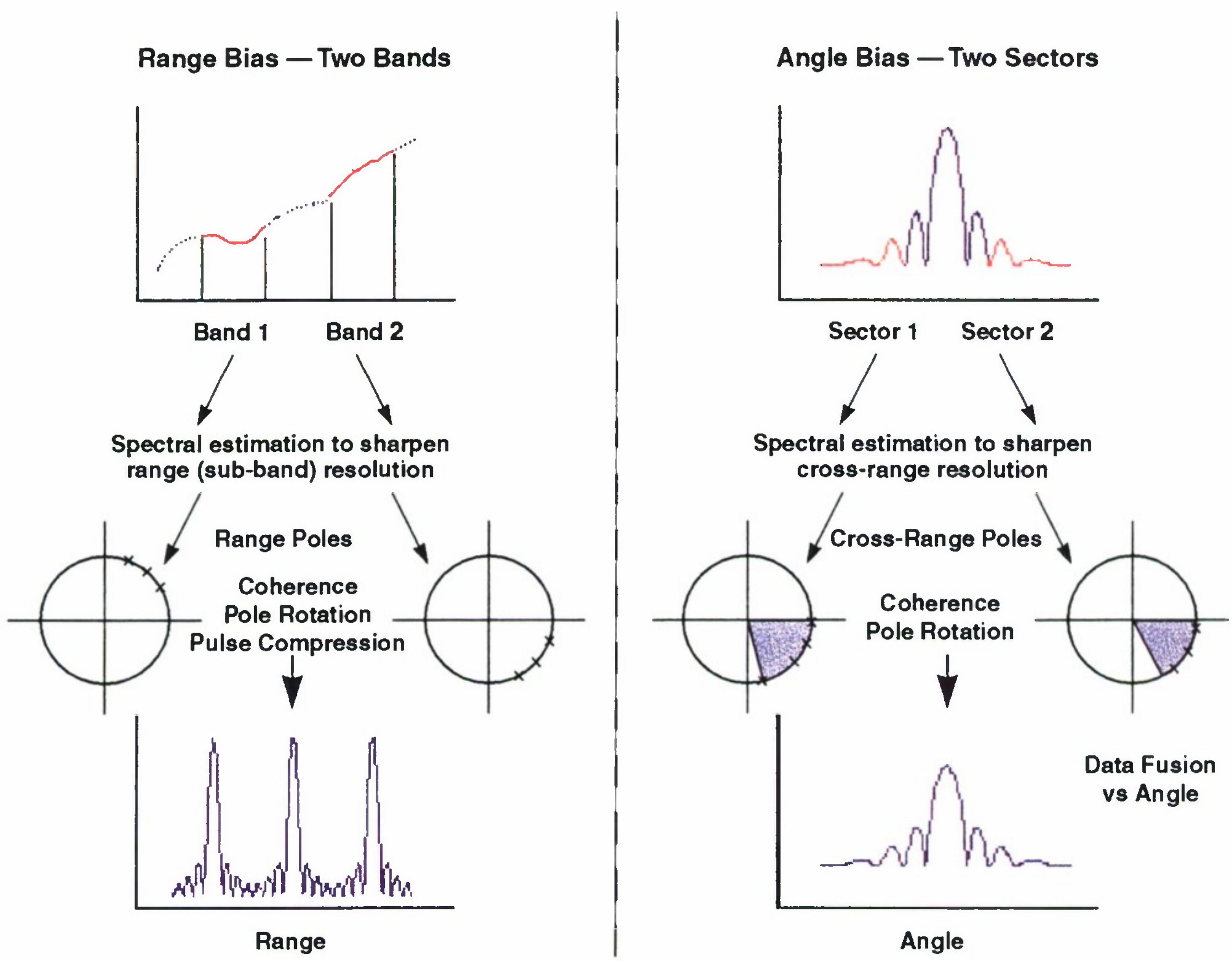

Figure 14. Coherence duality: range bias vs. angle bias.

4. SENSOR DATA FUSION EXAMPLES

This section provides examples that demonstrate the utility of using an image processor for sensor fusion. Considered are progressively more difficult (but also more realistic) target-scatter models, beginning with a constant-amplitude point-scatter model, progressing to three-dimensional physical targets, and ending with enhanced-fusion algorithms applied to static-range data. The targets considered are not comprehensive, but they are illustrative of the concepts and techniques that have been developed.

One goal of combining multisensor data is to achieve enhanced resolution and more comprehensive target characterization. The next subsection demonstrates that if the target model consists of M ideal constant-amplitude point scatterers, an efficient data-fusion algorithm that provides superresolution comparable to that achieved in [1] can be developed for two or more wideband sensors. This section begins by presenting this example, considers the case of narrowband sensors, and then extends the concept to more-physical targets.

4.1 CONSTANT-AMPLITUDE POINT-SCATTER MODEL (WIDEBAND FUSION)

4.1.1 Images from Single-Sensor Data and Conventional Processing of Multisensor Data

Consider a scenario in which two spatially separated sensors collect data on the target illustrated in Figure 15. To demonstrate that ultrawide-bandwidth wide-angle resolution is achievable by fusing multisensor data, the target chosen comprises five scatterers that are not totally resolvable by either sensor alone. It is most illustrative to depict the data-collection regions using the (u,v) space characterization introduced in Section 2.

It is assumed that each sensor acquires data in a different sector of (f,φ) space, as indicated in Figure 16. Table 2 lists the parameters for each sensor, as well as parameters for a hypothetical sensor with a bandwidth that spans those of sensors 1 and 2, plus a full rotation of look angles. The point scatterers for sensors 1 and 2 are not resolvable with either sensor by itself.

Figure 17 illustrates the image generated using wide-bandwidth/wide-angle data from a hypothetical sensor. The image in Figure 17 is the reference to which other images of this target are compared; it represents an optimal image that is achievable only by a hypothetical sensor. Processing methods used in this section and in Section 4.2 will be evaluated based upon how close their results match the reference image in Figure 17.

Figure 18 shows the image obtained from sensor 1 data using the conventional image processor defined by Equation (6). The bandwidth and angular span of the data from sensor 1 limit range and cross-range resolution to approximately 0.15 and 0.06 m, respectively. Because the spacing between all point sources is less than the range-resolution limits and the spacing between three of the point sources is less than the cross-range resolution limits, none of the target's five scatterers is resolved, and poor image quality results.

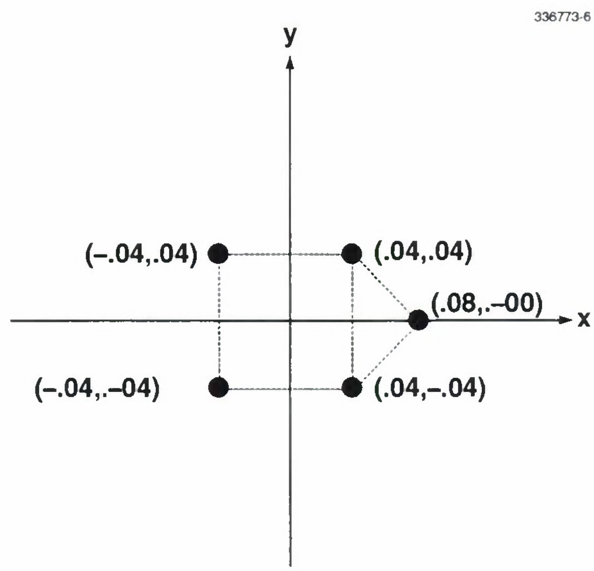

Figure 15. Geometry of target (meters).

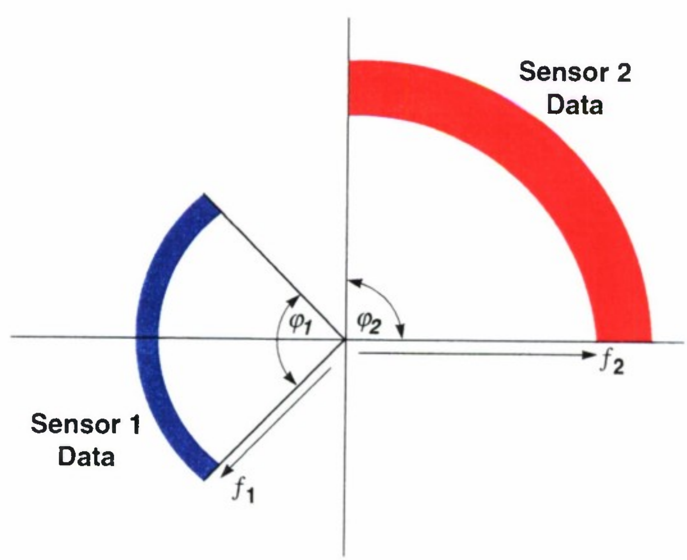

Figure 16. Scenario for collection of data from sensors 1 and 2.

TABLE 2
Sensor Parameters

Parameter	Sensor 1	Sensor 2	Hypothetical Wide-Bandwidth/ Wide-Angle Sensor
Frequency Band	3 to 4 GHz	9.5 to 10.5 GHz	3 to 10.5 GHz
Frequency Step Size	100 MHz	100 MHz	100 MHz
Observation Angles	155 deg $\leq \varphi_1 \leq$ 200 deg	40 deg $\leq \varphi_2 \leq$ 85 deg	0 deg $\leq \varphi \leq$ 359 deg
Angular Step Size	1 deg	1 deg	1 deg
Range Resolution	0.150 m	0.150 m	0.020 m
Unambiguous Range	1.5 m	1.5 m	1.5 m
Cross-Range Resolution	0.055 m	0.019 m	0.014 m
Unambiguous Cross Range	2.455 m	0.859 m	1.272 m

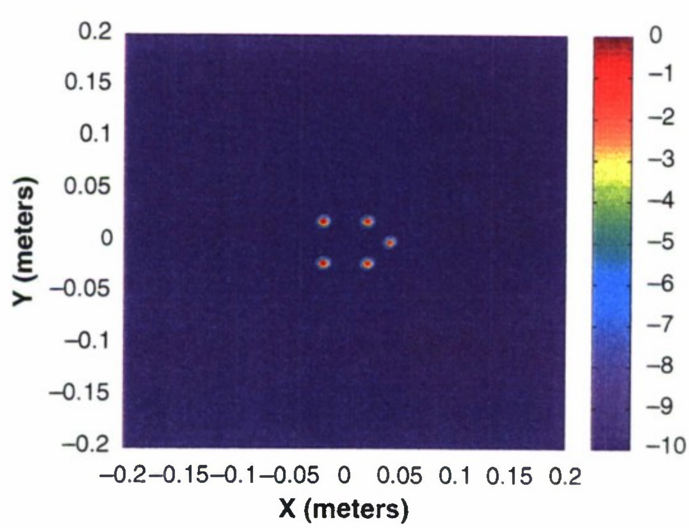

Figure 17. Image generated using data over frequency band 3 GHz $\leq f \leq$ 10.5 GHz *(*Δf = 100 MHz*) and aspect angles* 0 deg $\leq \varphi \leq$ 359 deg *(*$\Delta\varphi$ = 1 deg*).*

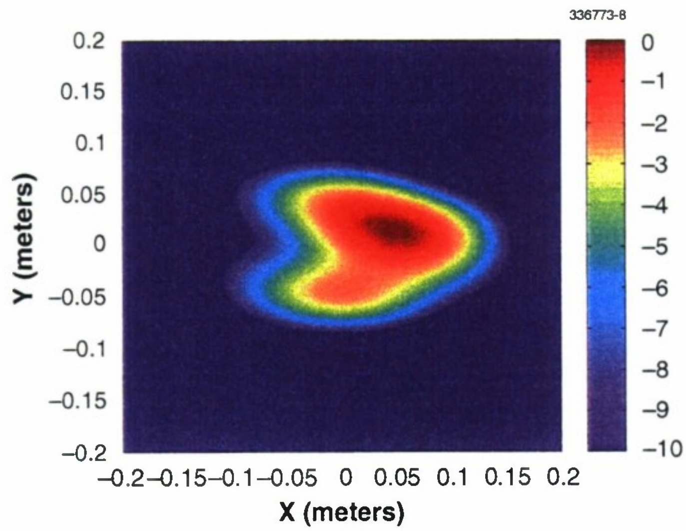

Figure 18. Frequency band 3 GHz $\leq f \leq$ 4 GHz , *aspect angles* 155 deg $\leq \varphi \leq$ 200 deg.

Figure 19 shows the image obtained from sensor 2 data. X-band data from sensor 2 provide range and cross-range resolution of 0.15 and 0.02 m, respectively. Scatterers are resolved in the cross-range direction; however, image quality is still poor because of inadequate range resolution.

Figure 20 shows the image obtained by directly combining data from sensors 1 and 2 using the image processor in Equation (24). Combining data from both sensors using the image integral in Equation (24) increases resolution (inasmuch as all five point sources are visible within Figure 20) but introduces many ambiguities because of gaps in the data. These ambiguities make it impossible to determine where the true scatterers are located. Figure 21 shows a magnification of Figure 20 and indicates the true location of the five point sources in the presence of the many ambiguities.

To significantly improve image quality, it will be necessary to fill in missing frequency and angle data either by obtaining more measurements or by using signal-processing methods. Section 4.1.2 develops an algorithm that extends the ultrawide-bandwidth processing techniques developed in [1] as a means for extrapolating the database for high-resolution imaging.

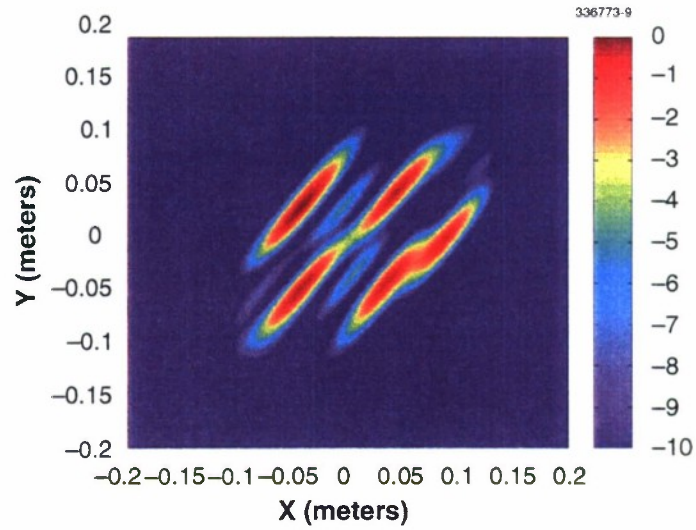

Figure 19. Frequency band 9.5 GHz $\leq f \leq$ 10.5 GHz , *aspect angles* 40 deg $\leq \varphi \leq$ 85 deg .

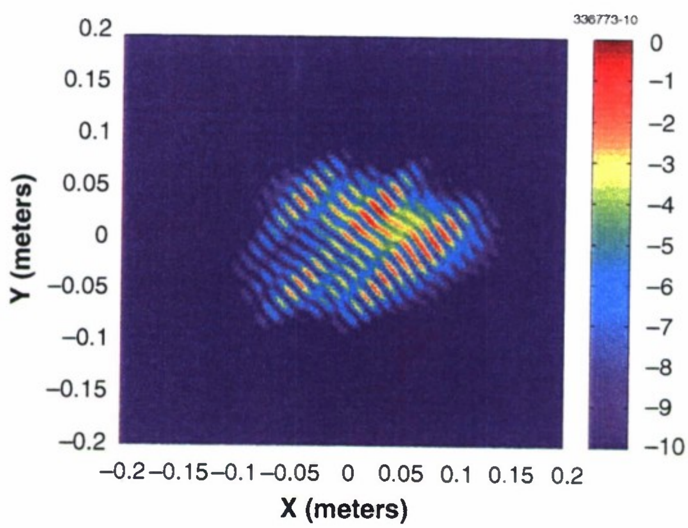

Figure 20. Image integral of Equation (24) is used to combine data from sensors 1 and 2.

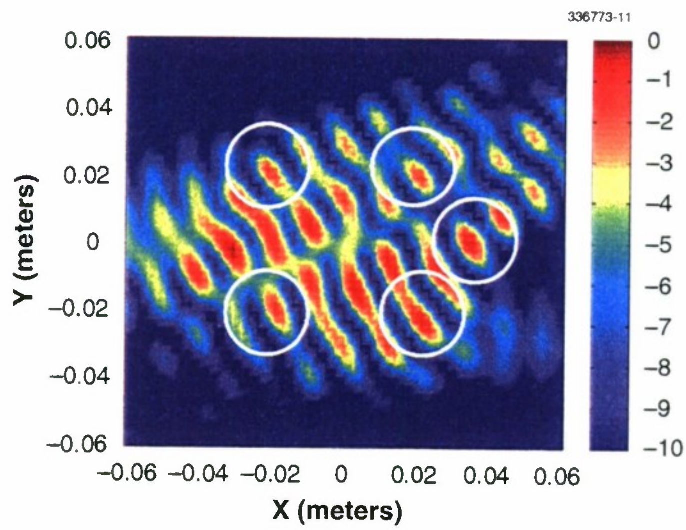

Figure 21. Magnification of Figure 20, showing resolution of point sources (enclosed in white circles).

4.1.2 Two-Dimensional Ultrawide-Bandwidth Processing

Section 2.1 showed that the radar response for targets containing M constant-amplitude pointlike scattering centers can be interpreted in terms of a two-dimensional target function $E(f,\varphi)$ written as

$$E(f,\varphi) = \sum_{m=1}^{M} \sigma_{c,m} e^{-j\frac{4\pi f}{c}(x_m \cos\varphi + y_m \sin\varphi)} \quad . \tag{41}$$

If $E(f,\varphi)$ is sampled in (f,φ) space at the grid point (f_n,φ_n), the samples of E are given by

$$E(f_n,\varphi_n) = \sum_{m=1}^{M} \sigma_{c,m} e^{-j\frac{4\pi f_n}{c}(x_m \cos\varphi_n + y_m \sin\varphi_n)} \quad . \tag{42}$$

Equation (42) shows that the samples of $E(f,\varphi)$ fall naturally into the two-dimensional polar-processing space illustrated in Figure 16. The radar interrogation frequency f corresponds to the "radius vector" in this space. The target viewing angle φ determines the azimuth angles of the target samples within the polar-processing space. In terms of Cartesian coordinates, the locations of the measurement samples are given by

$$u_n = \frac{4\pi f_n}{c}\cos\varphi_n \quad ,$$

$$v_n = \frac{4\pi f_n}{c}\sin\varphi_n \quad . \tag{43}$$

Equation (43) can be viewed as a change of variables from the polar coordinate system (f, φ) to Cartesian coordinates (u,v). With this change of variables Equation (42) becomes

$$E(u_n,v_n) = \sum_{m=1}^{M} \sigma_{c,m} e^{-j(x_m u_n + y_m v_n)} \quad . \tag{44}$$

Observe from Equation (44) that radar return signals from ideal constant-amplitude pointlike objects can be viewed as a superposition of two-dimensional sinusoids (waves) in (u,v) processing space. Processing data in (u,v) space significantly simplifies subsequent signal processing, as it allows the unknown parameters in $E(u_n,v_n)$ to be estimated accurately using the all-pole modeling techniques developed in [1]. To accomplish this, the data must be resampled corresponding to equispaced increments $(\Delta u,\Delta v)$, as discussed in Section 2. In Equation (44) the parameters (x_m,y_m) correspond to the locations of target points in the target fixed coordinate system (Figure 4), and (u_n,v_n) correspond to sample vectors in the polar-processing space. The primary signal-processing goal is to estimate the unknown target parameters that characterize E (i.e., M, x_m, y_m) by coherently processing all available radar measurements.

Assuming that N radar measurements are taken over a uniformly spaced set of frequencies and viewing angles, the components of the sample vector (u_n,v_n) may be written in terms of corresponding sample indices:

$$u_n = u_0 + \delta_u n_1 \ , \ n_1 = n \in \{0, \ldots, N-1\} \quad ,$$

$$v_n = v_0 + \delta_v n_2 \ , \ n_2 = n \in \{0, \ldots, N-1\} \quad . \tag{45}$$

The sampled function E in Equation (44) can then be written as

$$E(n_1,n_2) = \sum_{m=1}^{M} c_m \sigma_m e^{-j(x_m \delta_u n_1 + y_m \delta_v n_2)} = \sum_{m=1}^{M} a_m p_m^{n_1} q_m^{n_2} \quad , \tag{46}$$

where a_m denotes the complex-valued amplitude coefficients corresponding to the pole pairs (p_m,q_m). Thus $E(n_1,n_2)$ is equivalent to an all-pole signal model with poles having a magnitude of unity and angles that depend on the location of the point scatterers in the two-dimensional target fixed coordinate system.

Considering the discussion on polar formatting of data in Section 2.1, it is clear that Equation (44), sampled in uniform increments of (u_n,v_n), represents $E(f,\varphi)$ in a polar format. Thus, while polar formatting of data has traditionally been used for imaging applications because it produces focused images using the fast Fourier transform, it has now been shown that radar returns in a polar format can be interpreted as an all-pole model whose M poles correspond to M pointlike scatterers. This allows the extension of the one-dimensional pole formulations of the ultrawide-bandwidth problem to the two-dimensional frequency-angle case, which is accomplished used the following procedure:

1. Received radar data in (f,φ) space must be resampled onto a rectangular grid in (u,v) space, as shown in Figure 22.

2. Resampled data along horizontal lines are loaded into a block Hankel matrix $\mathbf{H}_u$, representing signal variations in u space (Figure 22).

3. Resampled data along vertical lines are loaded into a block Hankel matrix $\mathbf{H}_v$, representing signal variations in v space (Figure 22).

4. Each Hankel matrix $(\mathbf{H}_u,\mathbf{H}_v)$ is processed as described in Section 5 to determine the u-and v-direction poles, respectively. The pole locations are then optimized using a nonlinear least-squares method. The resulting two-dimensional all-pole model is given by

$$s(u,v) = \sum_{i=1}^{M_v} \sum_{i=1}^{M_u} a_{ij} p_i^u q_j^v \quad , \tag{47}$$

which can be equivalently written in matrix form as

$$\mathbf{S} = \mathbf{PAQ}^{\mathrm{T}} \quad . \tag{48}$$

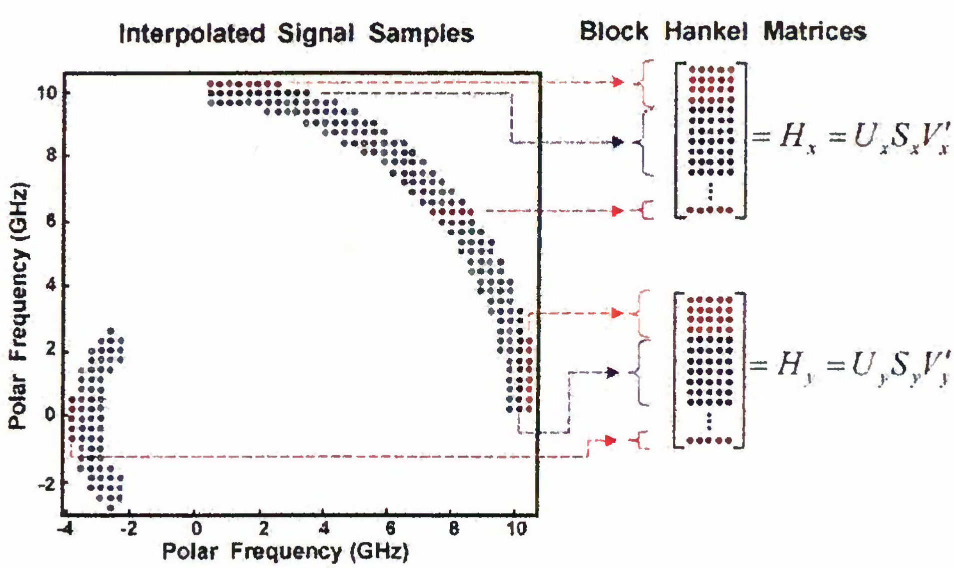

Figure 22. Pole estimation using two-dimensional root-MUSIC processing.

5. Estimate $\mathbf{A}$ in Equation (48) using a linear least-squares method. Thresholding applied to the elements of $\mathbf{A}$ allows the double-sum signal model of Equation (47) to be replaced by an approximate single-sum signal model written as

$$\tilde{s}(u,v) = \sum_{m=1}^{M} a_m p_m^u q_m^v \quad . \tag{49}$$

Figure 23 shows the image generated from sensor 1 and 2 data after two-dimensional ultrawide-bandwidth processing. A comparison of Figure 23 with the reference image of Figure 17 and the combined-data image of Figure 20 shows that two-dimensional ultrawide-bandwidth processing offers a significant improvement in image resolution over conventional processing of multisensor data.

The method described breaks down when there are not enough samples from a sensor to perform bilinear interpolation for polar formatting; for example, when one or both sensors are very narrowband. Section 4.2 introduces an alternative method for filling in missing data for narrowband sensors. The method to be described extends the data using an iterative approach.

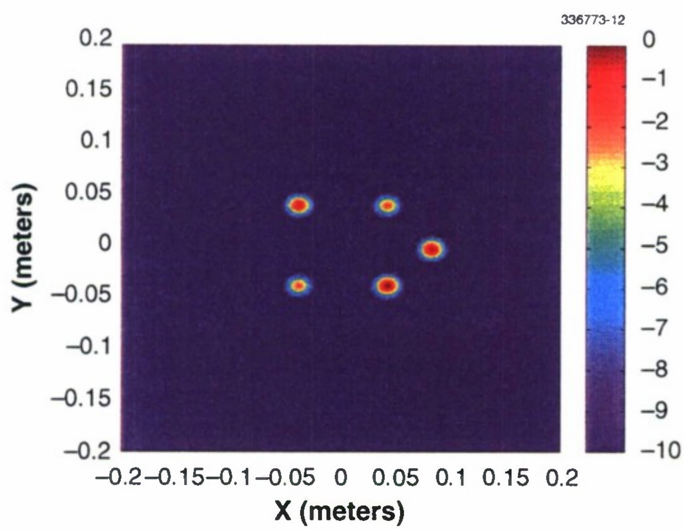

Figure 23. Image from combined sensor data after two-dimensional ultrawide-bandwidth processing.

4.2 CONSTANT-AMPLITUDE POINT-SCATTER MODEL (NARROWBAND FUSION)

For narrowband sensors the width of the frequency band over which data are obtained becomes very small, so there may not be enough samples to develop a Hankel matrix of sufficient rank to provide a good pole estimation. In this case it is useful to develop alternative methods for processing narrowband data. This section develops an iterative algorithm for enhancing the performance of the conventional image processor defined by Equation (6) for very narrowband wide-angle data. This iterative technique will be extended to physical targets in the next section.

It is assumed that data are available over perhaps a sparse subset of the interval $0 \le \varphi \le 2\pi$ and a narrow band of frequencies. Carrying out the image integral in Equation (6) over the known data sectors will provide a degraded image of the target model; however, generally the peaks of this image are ambiguous and/or close to the correct source locations. The method developed here uses these ambiguous sources to estimate (extend) $E(f,\varphi)$ outside the data regions. Then the integration in Equation (6) can be carried out over a much larger angular sector, providing better resolution of the actual sources that are present. The process can be carried out iteratively, with the anticipation that it will converge on the true source locations if the number of point sources is not too large.

The methodology consists of the following steps:

1. Construct an image from $\hat{E}(f,\varphi)$ using the image integral of Equation (6) over regions of known data and estimate scatterer locations $(\hat{x}_m, \hat{y}_m)$.

2. Revise $\hat{E}(f,\varphi)$ using estimated scatterer locations $(\hat{x}_m, \hat{y}_m)$ as follows:

$$\hat{E}(f,\varphi) = \begin{cases} E(f,\varphi), \text{ over } \varphi_1 \\ \sum_m A_m e^{j\frac{4\pi f}{c}\hat{x}_m \cos\varphi} e^{j\frac{4\pi f}{c}\hat{y}_m \sin\varphi}, \text{ outside } \varphi_1 \end{cases} . \tag{50}$$

3. Determine the values of A_m in Equation (50) by a least-squares fit to $E(f,\varphi_1)$ over φ_1.

4. Construct a new image over the larger sector using updated field estimates from Equation (50) and revise estimates of scatterer locations $(\hat{x}_m, \hat{y}_m)$.

5. Iterate on steps 1 through 4 to refine estimates of scatterer locations $(\hat{x}_m, \hat{y}_m)$.

The example shown to demonstrate this methodology uses known target-signature data measured at three frequencies, $3.95 \text{ GHz} \le f \le 4 \text{ GHz}$, $\Delta f = 25\text{MHz}$, and over an angular sector $\varphi_1 = -45 \text{ deg} \le \varphi \le 45 \text{ deg}$. The 1.2-m target comprises five point scatterers, as shown in Figure 24. This geometry is similar to that considered in the previous section, scaled by a factor of ten. The extended region is treated as $0 \le \varphi \le 2\pi$.

Figure 25 shows an image constructed using the known data $E(f,\varphi)$. The five scatterers and the general shape of the target are resolved within the image, but there are numerous ambiguities present that make it difficult to determine accurately where the true scatterers lie.

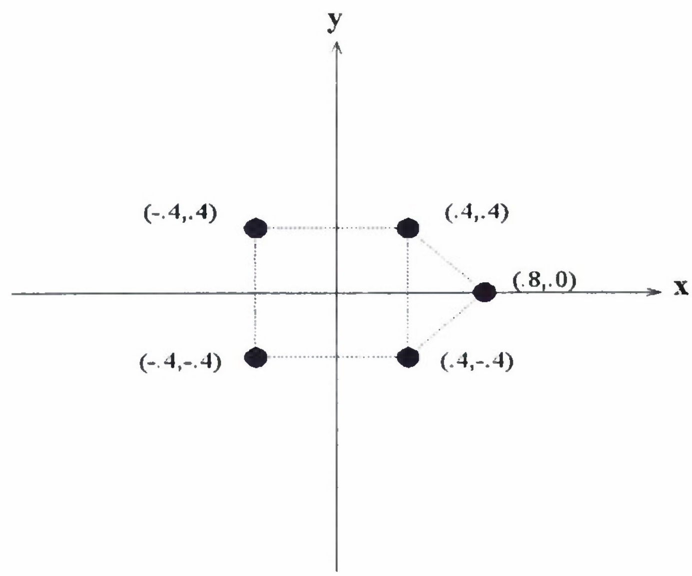

Figure 24. Five-point scatterer with overall length of 1.2 m.

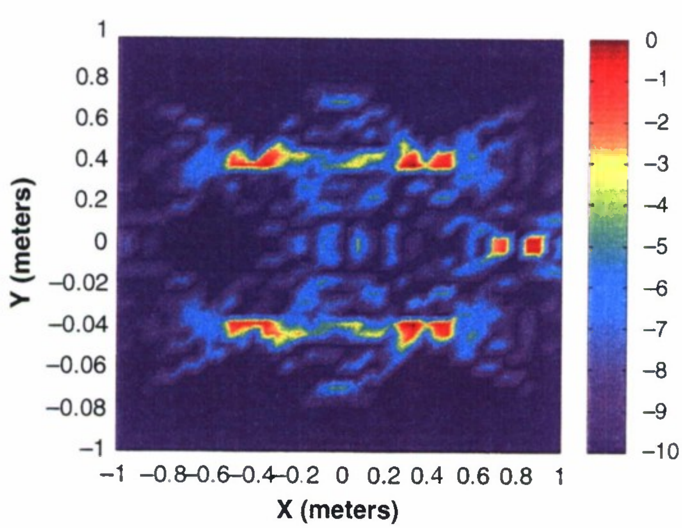

Figure 25. Image constructed from known data calculated at $3.95 \text{ GHz} \le f \le 4 \text{ GHz}$ *and aspect angles* $-45 \text{ deg} \le \varphi \le 45 \text{ deg}$.

The next step is to estimate scatterers $(\hat{x}_m, \hat{y}_m)$ by performing a search over the image of Figure 25 for the M largest peaks. The example uses $M = 6$. $\hat{E}(f,\varphi)$ is then revised as described in steps 2 and 3. Figure 26 shows the A_m values found in step 3.

Figure 27 shows the image generated from revised $\hat{E}(f,\varphi)$, showing a significant reduction in ambiguities. A second iteration is performed using Figure 27 to search for the M largest peaks, where now $M = 5$. Figure 28 shows the A_m values found in the second iteration of step 3. Figure 29 shows the image generated from revised $\hat{E}(f,\varphi)$ after the second iteration. Two iterations have achieved a significant improvement in the image; more iterations will offer no further enhancement.

The practicability of this technique depends on having enough data so that the estimates $(\hat{x}_m, \hat{y}_m)$ contain the positions of the actual scatterers and on the validity of the constant-amplitude point-scatter model over the entire region. Using this technique and those discussed in Section 4.1, a methodology can be developed for fusing sparse-angle, sparse-band data for narrow- and wideband sensors for the constant-amplitude point-scatter model. More physical-type targets are now considering using this framework.

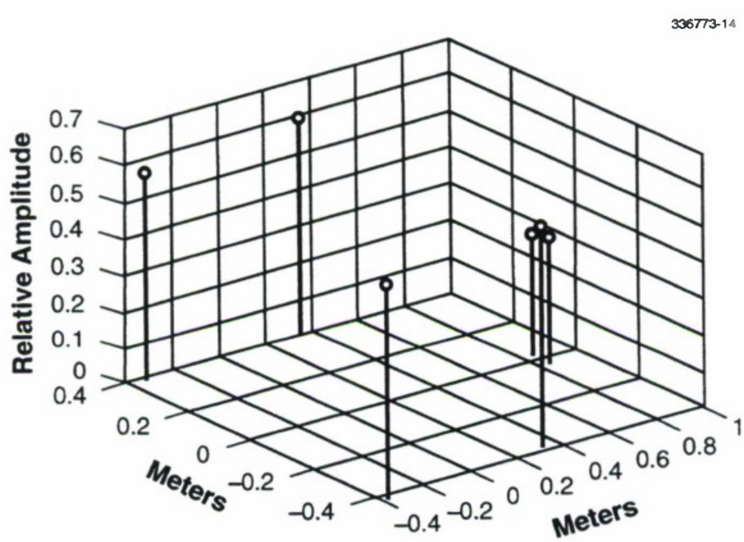

Figure 26. A_m values found from Equation (50) in step 3.

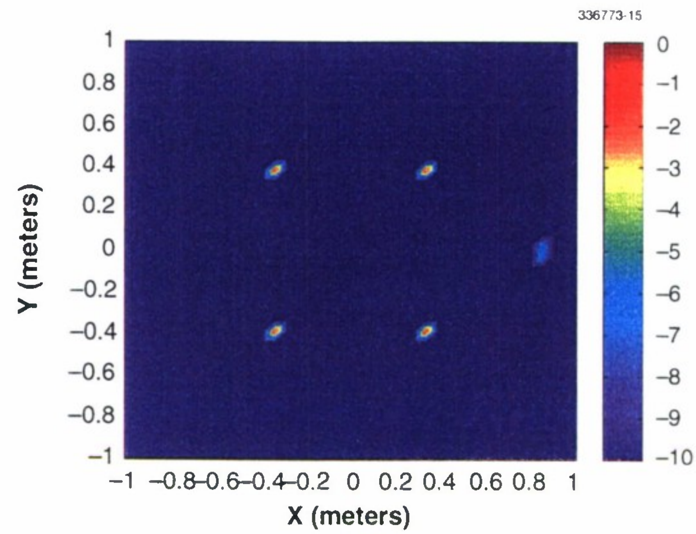

Figure 27. Improved image from extended data.

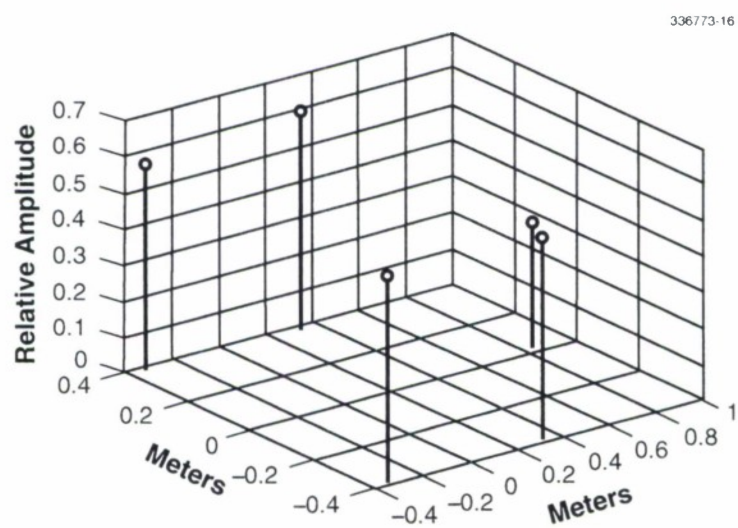

Figure 28. A_m values found from Equation (50) in second iteration of step 3.

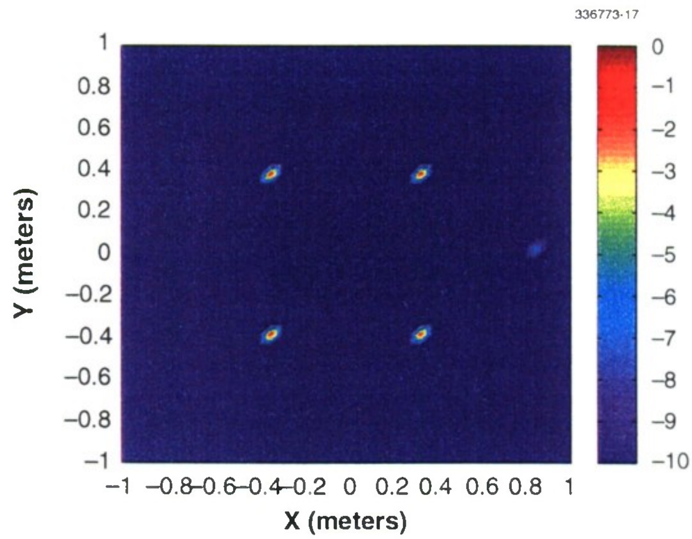

Figure 29. Improved image from extended data after second iteration.

4.3 EXTENSION TO PHYSICAL TARGETS

4.3.1 Narrowband Fusion Over Multiple Angular Sectors

The previous sections illustrate that for an ideal constant-amplitude point-scatter target it is possible to achieve robust sensor fusion over broad angular sectors for wide- and narrowband sensors using two-dimensional (u,v) space-processing techniques. The techniques shown allow for data interpolation between both sparse-angle sectors and frequency bands and extrapolation to an extended region of (u,v) space. The method's practicability lies in the constant-amplitude point-scatter approximation and its validity over wide angles and wide frequency bands. Unfortunately, real targets are much more complicated, and the constant-amplitude point-scatter model applies only over limited angular segments. The difficulty encountered when attempting to extend bandwidth-extrapolation techniques to the angular domain for real targets has been discussed by Moore et al. [3]. They point out that angular (aperture) extrapolation departs from bandwidth extrapolation in two ways: the nonlinear phase dependence due to range dependence on angle, and the large number (nonphysical) of constant-amplitude scattering centers required to characterize a specular response. They further point out that over limited regions, away from specular responses, one can achieve perhaps a factor-of-two to a factor-of-four increase in cross-range resolution. Thus the constant-amplitude point-scatter approximation is most severe when attempting to connect or interpolate data between widely spaced angular segments.

In general, *for a given look angle to the target*, the point-scatter model has broad applications; thus, the techniques developed in [1] are robust in allowing data fusion between frequency bands for sensors with a common look angle to the target. In fact, [1] demonstrates the validity of the all-pole frequency model over a wide range of targets of interest over limited angular sectors. The problem arises when extending these results to interpolating data between widely spaced angular sectors. Although the constant-amplitude point-scatter model is locally valid, the amplitude of the point-scatter model changes considerably between sectors, and the direct application of the techniques developed above to realistic targets breaks down, primarily because of three main effects:

1. Specular responses,
2. Diffraction from discontinuities,
3. Shadowing.

Specular Responses. Speculars occurring in the angular domain are analogous to the resonance effect in the frequency domain. An all-pole model with constant-amplitude coefficients is generally poor in modeling resonance phenomena, primarily because of the large dynamic range of the response. Thus constant-amplitude point-source models provide poor characterization of speculars.

Diffraction from Discontinuities. It is well known from the geometrical theory of diffraction [4] that the field scattered from a discontinuity on a scattering body is well modeled at high frequencies by a localized point source whose complex amplitude changes with frequency and angle. Thus for a given discontinuity located at the coordinate (x_m, y_m), the field scattered at a given polarization is characterized by

$$D_m(f,\varphi)e^{-jux_m}e^{-jvy_m} \quad , \tag{51}$$

where u and v are as defined in Equation (13). For a given φ_0, the variation of $D_m(f,\varphi_0)$ is typically well modeled by the f^{α} dependence considered in [1], where the exponent α is dependent on scatterer type. This forms the rigorous basis for the general validity of the all-pole frequency model; however, for some resonant scatterers (for example, a resonant antenna on a conducting body) the variation of $D_m(f,\varphi_0)$ versus frequency is not characterized well by f^{α}, but by a tuned resonant circuit response. In this case one would resort to a different basis expansion for $D_m(f,\varphi_0)$; fortunately, this resonance effect is atypical of the most common scattering feature types.

Unfortunately, for fixed-frequency f_0, the *typical* variation of $D_m(f_0,\varphi)$ versus φ is more analogous to the frequency-resonant scatterer case than the f^{α}-dependence case. To see this, consider the analytic expression characterizing $D_m(f,\varphi)$ for the two-dimensional wedge, denoted by $D(f,\varphi)$, which is illustrated in Figure 30:

$$D(f,\varphi) = \frac{D_0}{\sqrt{f}}\left[D_1 + \frac{1}{\cos\left(\frac{\pi}{n}\right) - \cos\left(\frac{2\varphi}{n}\right)}\right] \quad , \tag{52}$$

where D_0 and D_1 are constants, $n = (2 - \varphi_w)/\pi$, φ_w is the wedge angle, and transverse electric incidence to the wedge is assumed. For $\varphi = \varphi_0$, $D(f,\varphi_0) \approx f^{-0.5}$, which is well modeled by an f^{α} variation using

$\alpha = -0.$; however, for fixed f_0 the variation of $D(f_0,\varphi)$ versus φ is more complex. Observe that a specular response from the wedge geometry illustrated in Figure 30 occurs at two angles:

$$\varphi_1 = \frac{\pi}{2} \ ,$$

$$\varphi_2 = \frac{3\pi}{2} - \varphi_w = n\pi - \frac{\pi}{2} \ . \tag{53}$$

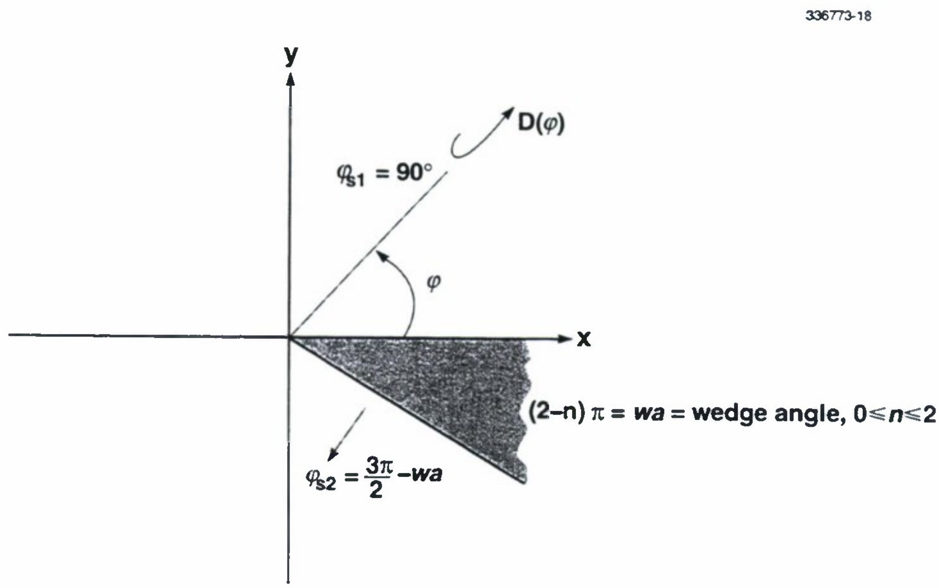

Figure 30. Geometry for wedge diffraction.

Using Equation (53), it is possible to rewrite Equation (52) in the form

$$D(f,\varphi) = \frac{D_0}{\sqrt{f}}\left[D_1 + \frac{1/2}{\sin\left(\frac{1}{n}(\varphi - \varphi_1)\right)\sin\left(\frac{1}{n}(\varphi - \varphi_2)\right)}\right] \ , \tag{54}$$

which clearly illustrates the singularity in $D(f,\varphi)$ at $\varphi = \varphi_1, \varphi_2$. Hence the analogy becomes clear that the variation of $D(f_0,\varphi)$ versus φ is more akin to a tuned-circuit resonance when compared with the frequency domain.

Observe that in regions about both sides of a given specular, $D(f_0,\varphi)$ is well modeled by a general expansion of the form

$$\hat{D}(f_0,\varphi) \approx C_1 + \frac{C_2}{\sin(\varphi - \varphi_s)} \quad , \tag{55}$$

where φ_s is the specular angle and C_1 and C_2 are constants that optimize the fit. Figure 31 illustrates the variation of $D(f_0,\varphi)$ for a 90-deg wedge and the approximation from Equation (55) that is used in later sections as a data-fusion basis function.

The functional form for $D_m(f_0,\varphi)$ given by Equation (55) is generally valid for localized scattering centers that inherently contribute to a specular response. This specular type of scattering is important because, once identified, it provides general information about the nature of the surfaces that are adjacent to the scatterer; e.g., flat or wedgelike types of interfaces. Other types of scattering centers are characterized by a functional form for $D(f,\varphi)$ that is generally different than Equation (54): one example would be a ridge or channel set on a curved conducting surface; in that case, the functional form for $D_m(f,\varphi)$ versus the angle would characterize the scattering pattern of the ridge or channel at the appropriate frequency. Thus a general parameter-based choice for the basis-expansion set must be robust enough to cover a variety of diffraction phenomena. Figure 32 illustrates various types of diffraction for a variety of example cases.

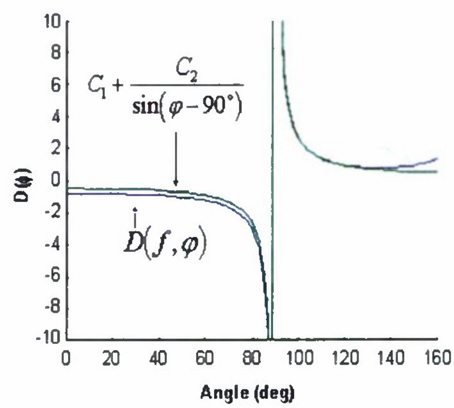

Figure 31. Diffraction from 90-deg wedge.

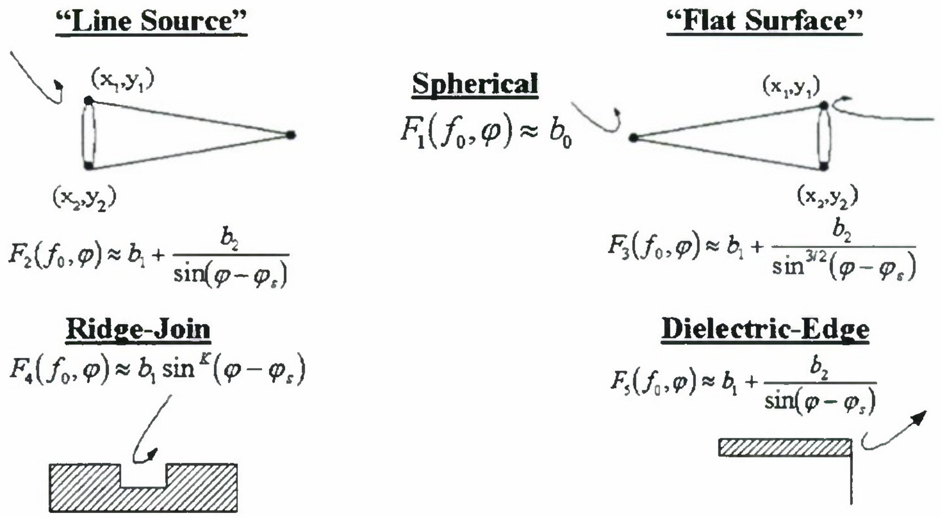

Figure 32. Example diffraction-basis functions.

An approximation that might be used to characterize the angular variation of $D(f_0,\varphi)$ for a fixed-frequency f_0 is also illustrated for each example. Although these examples are limited in scope, they provide a class of examples characterized by a more general form for $D(f_0,\varphi)$, given by

$$D(f_0,\varphi) \approx C_0 \frac{\sin^{k_0}(\varphi - \varphi_0)}{(\varphi - \varphi_0)} + C_1 + \frac{C_2}{\sin^{k_2}(\varphi - \varphi_{s_2})} \quad , \tag{56}$$

where k_0 and k_2 are constants that depend on the specific scatterer dimensions.

Shadowing. One basic premise of the geometrical theory of diffraction is that radiation or scattering to a particular point in space occurs primarily from scattering sources visible to the far-field observation point; thus, when fusing signature data from two different look angles, care must be taken to isolate scatterers visible to both sensors. The typical approach to this problem, used in extended coherent processing of single-sensor radar data over wide angles, is to limit coherent processing to 90-deg sectors, assuring the existence of at least some number of common scattering centers. Shadowing is of particular concern in mutual coherence compensation for widely spaced sensors, which will be addressed further in Section 4.3.3.

4.3.2 A Simple Example: Two-Dimensional Strip (Narrowband)

Perhaps the simplest deviation from the constant-amplitude two-point scatterer is the two-dimensional strip illustrated in Figure 33.

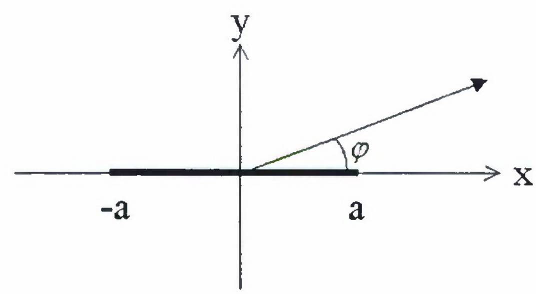

Figure 33. Geometry of a two-dimensional strip.

Relative to the three physical effects considered in the previous section, the strip exhibits specular and diffraction effects but no shadowing. For simplicity, the strip of width $2a$ is oriented on the x-axis of the x-y coordinate system so that backscatter from the strip is given by $E(f,\varphi)$, where φ is the standard azimuthal angle variable. Observe that for any look angle away from specular, the strip appears as a two-point scatterer; however, a constant-amplitude two-point scatter model will fit the data over only a limited angular sector. Using the geometrical theory of diffraction and the strip diffraction coefficient given by Equation (54), with $n = 2$, the backscattered field $E(f,\varphi)$ can be written in the form

$$E(f,\varphi) = D_1(f,\varphi)e^{+jua} + D_2(f,\varphi)e^{-jua} \quad , \tag{57}$$

where, as before, $u = \frac{4\pi f}{c}\cos\varphi$, and $D_1(f,\varphi)$ and $D_2(f,\varphi)$ are given by

$$\begin{aligned} D_1(f,\varphi) &= \frac{D_0}{\sqrt{f}}\left[1 + \frac{1}{\cos\varphi}\right] \quad , \\ D_2(f,\varphi) &= \frac{D_0}{\sqrt{f}}\left[1 - \frac{1}{\cos\varphi}\right] \quad . \end{aligned} \tag{58}$$

Observe that for any given angle $\varphi = \varphi_0$, the field amplitude varies as $f^{-0.5}$. The "real part" of the variation of $E(f,\varphi)$ for $\varphi_0 = 45$ deg is shown in Figure 34 and is characteristic of the f^{α} frequency behavior; however, for fixed-frequency $f = f_0$, the angular variation of $E(f,\varphi)$ is considerably different in nature, characteristic of a resonance as the field passes through the specular region, as illustrated in Figure 35. This duality is made clear by comparing Figure 34 with Figure 35, for which f_0 has been chosen such that $2a/\pi = 10$. In the former case, for fixed φ_0, the field variation is clearly modeled by a two-pole point-scatter model over the entire frequency band. The inability of a constant-amplitude all-pole model to model the angular field variation over broad angular regions is also evident from Figure 35.

Sector Processing: Narrowband Data. Consider now the case where data are available over two angular sectors that may be sparsely separated. The special case is considered where the field scattered in the observed sector regions is characterized by the same specular response. It has been shown qualitatively that an all-pole angle model is capable of characterizing the field variation over a limited angular sector; to quantify this effect, consider the field variation from each scattering center given by Equation (51) and approximate the variation of $D_m(f_0,\varphi)$ according to

$$D_m(f_0,\varphi) \approx D_0 e^{-\alpha_m \varphi} \quad . \tag{59}$$

Then the field variation that results from this localized scattering center is given by

$$E_m(f_0,\varphi) \approx D_0 e^{-\alpha_m \varphi} e^{-j\frac{4\pi f_0}{c} x_m \cos\varphi} e^{-j\frac{4\pi f_0}{c} y_m \sin\varphi} \quad . \tag{60}$$

Assuming $\varphi = \varphi_0 + n\Delta\varphi$ and for $n\Delta\varphi \ll 1$, Equation (60) takes the form of an all-pole model in $\Delta\varphi$:

$$E_m(f_0, \varphi_0 + n\Delta\varphi) \approx D_0 e^{-\alpha_m \varphi_0} e^{-j\frac{4\pi f_0}{c} x_m \cos\varphi_0} e^{-j\frac{4\pi f_0}{c} y_m \sin\varphi_0} (p_m)^n \quad , \tag{61}$$

where the pole p_m is given by

$$p_m = e^{+j\frac{4\pi f_0}{c} x_m \Delta\varphi \sin\varphi_0} e^{-j\frac{4\pi f_0}{c} y_m \Delta\varphi \cos\varphi_0} e^{-\alpha_m \Delta\varphi} \quad . \tag{62}$$

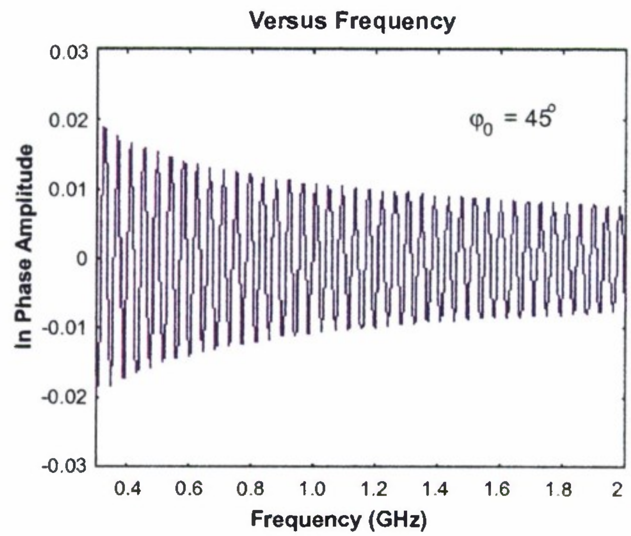

Figure 34. Scattered field from two-dimensional strip as a function of frequency.

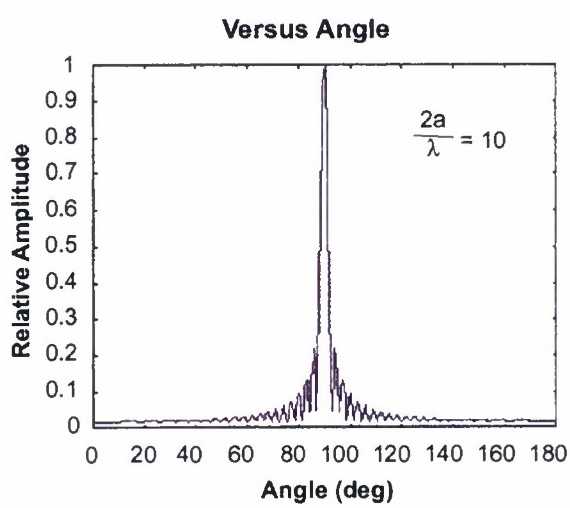

Figure 35. Scattered field from two-dimensional strip as a function of aspect angle.

Rewriting the pole p_m in terms of the cross-range resolution gives

$$\rho_{CR_m} = \rho_m \sin(\varphi_m - \varphi_0) \quad , \tag{63}$$

where $x_m = \rho_m \cos\varphi_m$ and $y_m = \rho_m \sin\varphi_m$, which gives

$$p_m = e^{j\frac{4\pi f_0}{c}\Delta\varphi\rho_{CR_m}} e^{-\alpha_m \Delta\varphi} \quad . \tag{64}$$

Thus the scatterers can be isolated in cross range using local all-pole spectral-estimation techniques, and the field variation can be characterized using a local all-pole model approximation. However, when compared with the exponential approximation f^{α} for the all-pole frequency model, the variation of α_m will be considerably larger, and the poles will be displaced a considerable distance off the unit circle.

The limitation on all-pole modeling over a broad angular sector is quantified by a simple example. Consider two sectors, $\varphi_0 = 40$ deg and $\varphi_0 = 80$ deg, each with a sector size of 12 deg. The poles associated within each sector are each estimated separately by using the technique described in [1]. The localized all-pole model fit to each data set, assuming two poles per sector, is illustrated in Figure 36. The all-pole model fit is clearly quite good over each sector; note in particular the exponential growth associated with the field in sector 2. Given for comparison is the all-pole approximation to the field over the entire region containing the two sectors (34 to 86 deg). The fit using a simple all-pole model to cover the entire region is poor overall and favors the sector where the field is strongest. The next section considers the fusion problem in joining the two sectors.

A Specular-Based Diffraction Basis-Expansion Set. The previous section demonstrates that a single all-pole model is not capable of representing the field variation for the two-dimensional strip over a broad angular sector. This is to be expected, particularly given the development in Section 4.2, where it was shown that a large number of poles are required to characterize an M-point scatter model over a broad angular sector and that the number approaches $(4\pi|r|_{\max})/\lambda$ as the angular sector approaches 2π. It was for precisely that reason that the transformation was made to (u,v) processing space, where a constant-amplitude scatterer is characterized by a single pole. Clearly, if a common model is to be found for interpolating data between angular sectors for realistic targets, a different basis set is needed.

To develop a set of basis functions appropriate to the angle-interpolation problem, refer to Equation (55), where it was demonstrated that the constants C_0, C_1, C_2, and a specular location φ_s are adequate to characterize the angular variation of $D_m(f_0,\varphi)$ over regions including the specular. Begin with the general expansion for $E(f,\varphi)$ determined by the geometrical theory of diffraction:

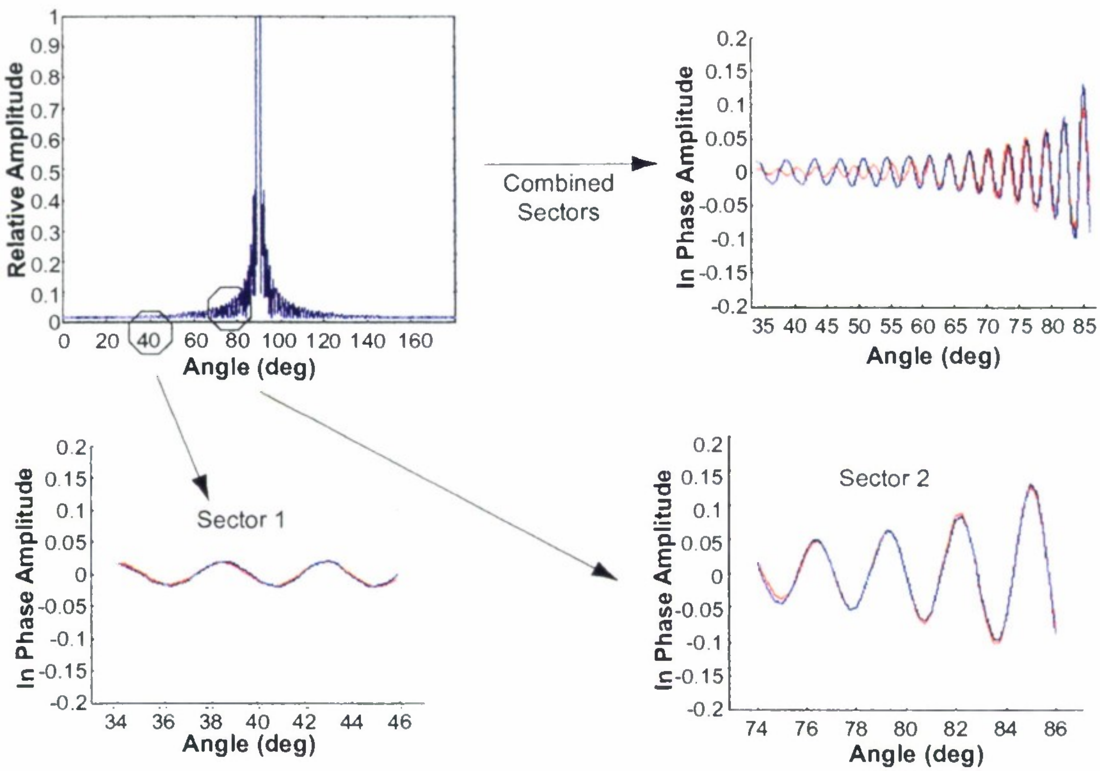

Figure 36. All-pole model for localized angular sectors.

$$E(f,\varphi) = \sum_{m=1}^{M} D_m(f_0,\varphi)e^{-jux_m}e^{-jvy_m} \quad . \tag{65}$$

Generalizing Equation (55) to the case of the m^{th} scattering center gives

$$E(f,\varphi) = \sum_{m=1}^{M} \frac{1}{\sqrt{f}}\left[C_{1,m} + \frac{C_{2,m}}{\sin(\varphi - \varphi_{s,m})}\right]e^{-jux_m}e^{-jvy_m} \tag{66}$$

at any given frequency $f = f_0$. Equation (66) is general enough to characterize the field variation over broad angular regions for either constant-amplitude or specular-dominant scattering. Consider, for example, the two-sector strip example given previously. Figure 37 illustrates the match to the data over the 34- to 86-deg sector at $f_0 = 3$ GHz using the single all-pole angle model of Figure 36 vs. that obtained using the diffraction-based basis set defined by Equation (66). The data match using the diffraction basis set essentially overlays the data over this broad angular region.

There is clearly a drawback to using the expansion basis set defined by Equation (66): the location of the specular appears as a nonlinear parameter. There are two solutions to this dilemma: the first is to estimate φ_s by nonlinear iteration of the fit to the data set to obtain the best match; the second is to estimate φ_s from other information, such as for a tumbling target rotating through a large number of sectors, where the speculars occur directly in the data. The first approach is pursued here. As a starting point to this nonlinear iteration, it is possible to estimate φ_s from the all-pole model obtained for each sector.

Consider the local approximation fitting the pole model to the diffraction basis set

$$D_0 e^{-\alpha_m \varphi} \approx C_{1,m} + \frac{C_{2,m}}{\sin(\varphi - \varphi_s)} \quad . \tag{67}$$

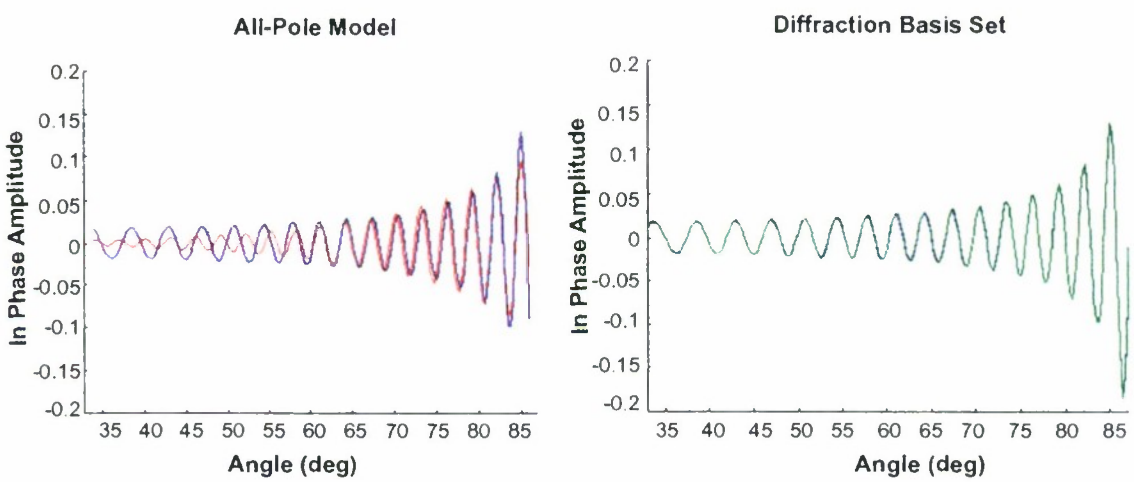

Figure 37. All-pole model and diffraction-basis set.

Assuming the second term dominates the exponential growth of the all-pole model, it can be shown that an estimate of φ_s is given by

$$\hat{\varphi}_s \approx \varphi_0 + \tan^{-1}\left(\frac{1}{\alpha_m}\right) \quad , \tag{68}$$

where φ_0 denotes the center of the angular sector under consideration. The closer φ_0 is to φ_s, the more correct the estimate. This initial estimate is used for φ_s in later sections on data fusion.

In general, the diffraction coefficient $D(f,\varphi)$ is a function of both frequency and angle. As discussed earlier, for fixed $\varphi = \varphi_0$, $D(f,\varphi)$ is well modeled by an f^{α} frequency-dependence. The exponential function $e^{-\beta f}$ can be found that best matches this f^{α} frequency-dependence over a wide frequency range [5], which provides the basis for the all-pole ultrawide-bandwidth model developed in detail in [1]. Using this exponential frequency-dependence, Equation (66) can be rewritten in the form

$$E(f,\varphi) = \sum_{m=1}^{M} e^{-\beta_m f}\left[C_{1,m} + \frac{C_{2,m}}{\sin(\varphi - \varphi_{s,m})}\right] e^{-jux_m} e^{-jvy_m} \quad , \tag{69}$$

where β_m denotes the assumed exponential frequency-dependence of the m^{th} scatterer. As it stands, Equation (69) contains β_m as a nonlinear parameter that is in general difficult to estimate for the general case where both f and φ are considered variable. For any given angle $\varphi = \varphi_0$, the exponential term $e^{-\beta_m f}$ may be interpreted as a complex pole in frequency space, and the parameter β_m is estimated directly from the spectral-estimation process. This approach can be used to process sparse multiband data over broad angular sectors as long as the angular variation of the measured data set is continuous (e.g., as for a spinning or tumbling target). In this case the poles associated with the expansion of Equation (66) are functions of angle and change with each processed pulse.

For the more general case of fusing data over sparsely located angular sectors and sparse-band sensors, the basis set given by Equation (69) must be used, and β_m is not so easily determined. Noting that a linear approximation to $e^{-\beta_m f}$ is generally valid over broad frequency ranges, as the frequency variation for other than resonant scatterers is weak, circumvents these difficulties. In this case $e^{-\beta_m f}$ is approximated in the form

$$D_0 e^{-\beta_m f} \approx D_0 - D_0 \beta_m f \quad . \tag{70}$$

Using Equation (70) in Equation (69) leads to the desired basis-expansion set:

$$E(f,\varphi) = \sum_{m=1}^{M} \left[C_{1,m} + \frac{C_{2,m}}{\sin(\varphi - \varphi_{s,m})}\right] [C_{3,m} + C_{4,m} f] e^{-jux_m} e^{-jvy_m} \quad . \tag{71}$$

Assuming $\varphi_{s,m}$ is estimated independently, for example using Equation (68), Equation (71) leads to a linear set of equations when $E(f,\varphi)$ is sampled at $f = f_n$, $\varphi = \varphi_k$. An algorithm is now presented for estimating the parameters in Equation (71) from a measured data set.

Image Processing and Data Fusion. Consider now the problem of estimating the parameters associated with the diffraction-based expansion given by Equation (71) when data are available over multiple angular sectors at different frequency bands. The approach is iterative, analogous to the approach to the constant-amplitude point-scatterer model in Section 4.2. This section considers only the multifrequency narrowband problem; it is directly extendable to the wideband case when broadband sector data are available. The approach is as follows:

1. Determine the all-pole model over each sector (or each subsector, for wide-angle data):

   a. Determine the scatterer locations and complex amplitudes A_m, obtained by a fit to the data over a given sector,

   b. Estimate the nearest specular $\varphi = \varphi_s$, one for each sector.

2. Form a sequence of images, one for each sector, as defined in Figure 12:

   a. Let (x_p,y_p) denote a pixel image point.

   b. Threshold the data according to

   $$\text{If } |A_m|^2 > T_0 \text{ , set } |A_m|^2 = T_0 \text{ ; } T_0 \text{ is a threshold parameter.} \tag{72}$$

   c. Form the sector image for each scatterer ρ_{CR_m}, determined for the sector φ_0 according to

   $$I_q(x_p,y_p) = \begin{cases} |A_m|^2, & \left|y_p - x_p \tan\varphi_0 - \dfrac{\rho_{CR_m}}{\cos\varphi_0}\right| < \varepsilon \\ 0, \text{ otherwise} & \end{cases} , \tag{73}$$

   where ε is a small number, on the order of a pixel-cell size.

3. Add the sequence of cross-range images

   $$I(x_p,y_p) = \sum_{Sectors} I_q(x_p,y_p) \quad . \tag{74}$$

4. Estimate the locations of the scatterers (x_m,y_m) from the peaks of the image $I(x,y)$.

5. Perform a least-squares fit to the data over the given sectors according to

$$E(f_k,\varphi_n) = \sum_{m=1}^{M}\left[C_{1,m} + \frac{C_{2,m}}{\sin(\varphi_n - \varphi_{s,m})}\right][C_{3,m} + C_{4,m}f_k]e^{-ju_{k,n}x_m}e^{-jv_{k,n}y_m} \quad . \quad (75)$$

6. Iterate the solution on the parameter $\{\varphi_{s,m}\}$.
7. Interpolate (fuse) the data over data gaps.

The image-formation algorithm enumerated above is similar in concept to the back-projection or layergram technique using the Radon transform, which is discussed in detail in [5]; however, it is different in three critical ways:

1. The subsector cross-range profile is obtained using a high-resolution spectral estimation technique and allows for complex poles; i.e., signal growth or decay over the sector.
2. The poles as determined are weighted according to the data fit described in 1(a) above; thus, ambiguous poles are eliminated.
3. Thresholding the data provides a much greater dynamic range for isolating closely spaced sources.

Example 1: Sparse-Angle Single-Band Data. Consider the strip example treated previously, where data are collected by two sensors over each of the two sectors 34 to 46 deg and 74 to 86 deg. The sensors are assumed to operate over the same frequency bands. The results of the various steps of the process outlined above are illustrated in Figure 38. The upper-left plot of Figure 38(a) shows the variation of the field magnitude over the 0- to 90-deg interval. To form an unambiguous image of the two edge points of the strip, subdivide each sector into two additional sectors, treating the known data effectively as four sectors, each 6-deg wide.

$$\begin{aligned} &\text{Sector 1 (34 to 40 deg)} \rightarrow \varphi_0 = 37 \text{ deg} \\ &\text{Sector 2 (40 to 46 deg)} \rightarrow \varphi_0 = 43 \text{ deg} \\ &\text{Sector 3 (74 to 80 deg)} \rightarrow \varphi_0 = 77 \text{ deg} \\ &\text{Sector 4 (80 to 86 deg)} \rightarrow \varphi_0 = 83 \text{ deg} \end{aligned} \quad . \quad (76)$$

The data fit using the all-pole model for each subsector is illustrated in Figure 38(b); the fit is essentially that of four separate sectors superimposed on the plot and is nearly identical to the original data. To estimate the specular location, use Equation (68), choosing the α_m that corresponds to the pole with the largest amplitude in the local fit to the data and for which the approximation leading to Equation (68) is most accurate. The results produce a value of $\hat{\varphi}_s = 90.1$ deg. Table 3 illustrates the value of $\hat{\varphi}_s$ obtained from each subsector and all values of α. The approximation improves as $\varphi_0 \rightarrow$ specular. A closer examination shows that those poles that are in considerable error in predicting a specular are not used in the data fit over that sector.

Figure 38(c) illustrates the initial image obtained using Equation (74), where the peaks at $x = \pm 1$ and $y = 0$ are evident, as are the ambiguities that occur. This image is thresholded to a given number of maxima, and these potential source locations are used in a least-squares fit to the data, defined by Equation (75). The fused signature data obtained from this fit are illustrated in Figure 38(d). The agreement is very good, both in the interpolated region and in the extrapolated region outside the sectors. Closer examination shows that only the image points at $x = \pm 1$ contribute significantly to the data fit.

An enhanced image of the target can be obtained using the fused data, by applying the cross-range imaging algorithm defined by Equation (73) to the fused data set. The result is shown in Figure 39(b). Observe that over the (30-deg, 80-deg) sector, the dominant scattering occurs from the edge located at (–1,0), which is closest to the far-field data region; thus, the enhanced image provides a measure not only of the scatterer location, but also of its relative contribution to the data-fusion process over the sector under consideration. The high-resolution image can be compared with images obtained from the image integral using the original sector data only, as illustrated in Figure 39(a).

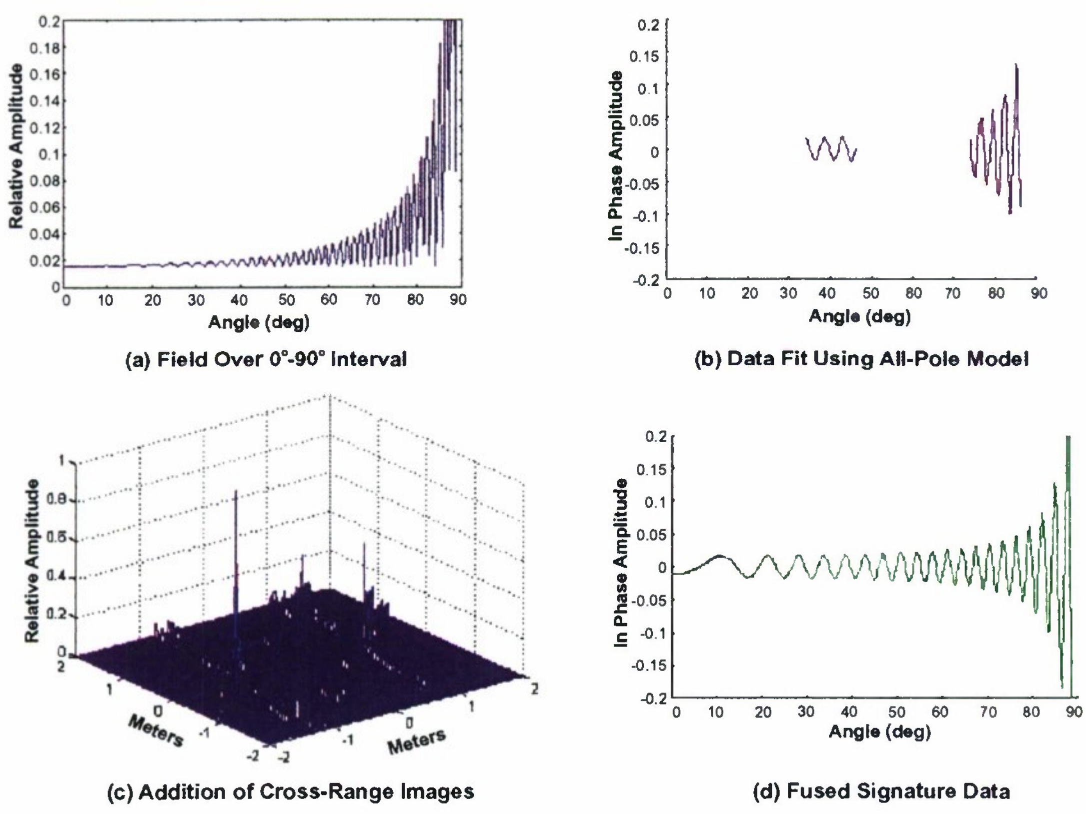

Figure 38. Data fusion for two-dimensional strip (Example 1).

TABLE 3
Estimation of Specular Locations

Sector	φ_0 (deg)	α	$\hat{\varphi}_s$ (deg)
1	37	−0.49 −5.37	100.7 47.5
2	43	−0.53 −3.77	104.9 51.83
3	77	−3.67 −5.76	92.2 86.8
4	83	−8.1 −10.3	90.1 88.5

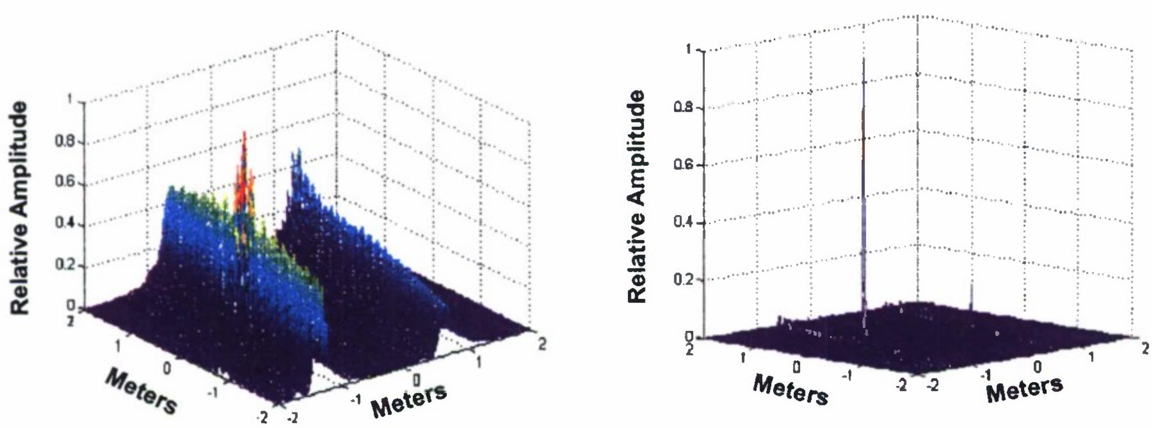

(a) Conventional Image

(b) Enhanced Image

Figure 39. Conventional and enhanced images of two-dimensional strip using fused data (Example 1).

Example 2: Sparse-Angle Multiband (Narrowband) Data. The second example considers data fusion for sensors operating over different frequency bands and located on either side of the specular region as defined below:

$$\text{Band 1 } (f_0 = 1.5 \text{ GHz}) \begin{cases} \text{Sector 1 } (37 \text{ to } 43 \text{ deg}) \rightarrow \varphi_0 = 40 \text{ deg} \\ \text{Sector 2 } (69 \text{ to } 75 \text{ deg}) \rightarrow \varphi_0 = 72 \text{ deg} \end{cases} ,$$

$$\text{Band 2 } (f_0 = 3 \text{ GHz}) \begin{cases} \text{Sector 3 } (130 \text{ to } 136 \text{ deg}) \rightarrow \varphi_0 = 133 \text{ deg} \\ \text{Sector 4 } (157 \text{ to } 163 \text{ deg}) \rightarrow \varphi_0 = 160 \text{ deg} \end{cases} . \tag{77}$$

This case attempts to fuse the data over the entire region (0 deg, 180 deg) at each of the two sensor bands. The following assumptions are made for simplicity: an L-band sensor $(f_0 = 1.5 \text{ GHz})$ over sectors 1 and 2 and an S-band sensor $(f_0 = 3 \text{ GHz})$ over sectors 3 and 4.

Figure 40(a) illustrates each sector's match to the "real part" of the data at each frequency using the cross-range poles estimated using the techniques in [1]. Using the value of α associated with the dominant pole over the four sectors, obtain $\hat{\varphi}_s \approx 94.6$ deg from Equation (78). The cross-range image is illustrated in Figure 40(b), where the peaks at $x = \pm 1$ and $y = 0$, as well as several ambiguous peaks, are evident. In practice, after thresholding the image, the image-peak search algorithm selects multiple peak locations. The resultant variation of the fused data is illustrated in Figure 40(c) at S-band and in Figure 40(d) at L-band. The enhanced image using the fused data (omitting the specular region) is shown in Figure 41(b), as compared with the conventional image that uses the sector data only, shown in Figure 41(a).

Clearly, the fused data's fit over each band is generally good and is degraded only in the region of the error in the estimate of the specular. The data fit could be improved by iterating the solution over the parameter $\hat{\varphi}_s$, as indicated in step 5 of the fusion process. To prevent a clustering of image points in any given region, the image data have been filtered about the maximum image point according to

$$|I(x,y)|_{MAX} \text{ over } |\Delta| \leq \Delta_0 \quad , \tag{78}$$

where $\Delta_0 = 2\lambda$ has been chosen for this example, effectively limiting the resolution of the source-location algorithm used to spacings greater than 2λ.

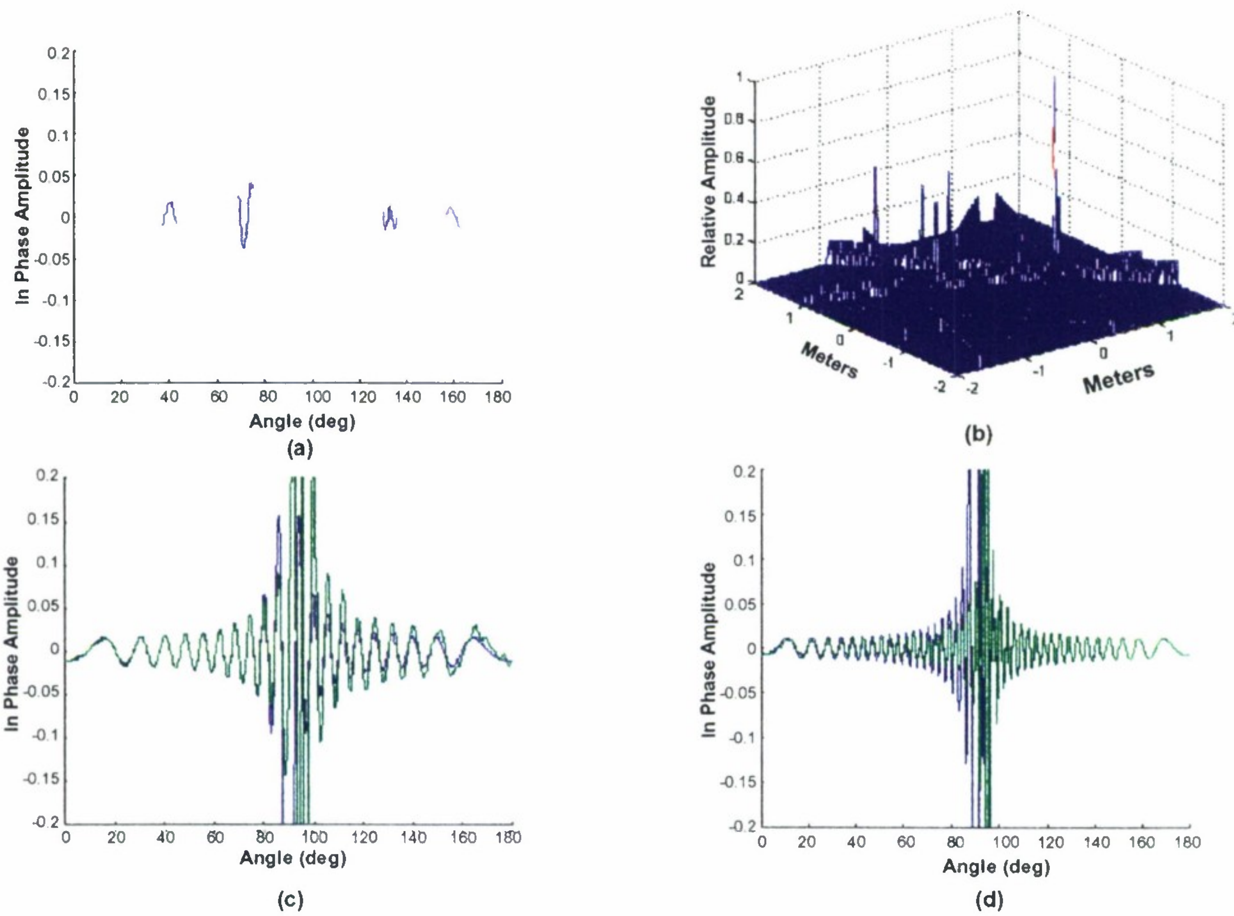

Figure 40. Data fusion for two-dimensional strip (Example 2).

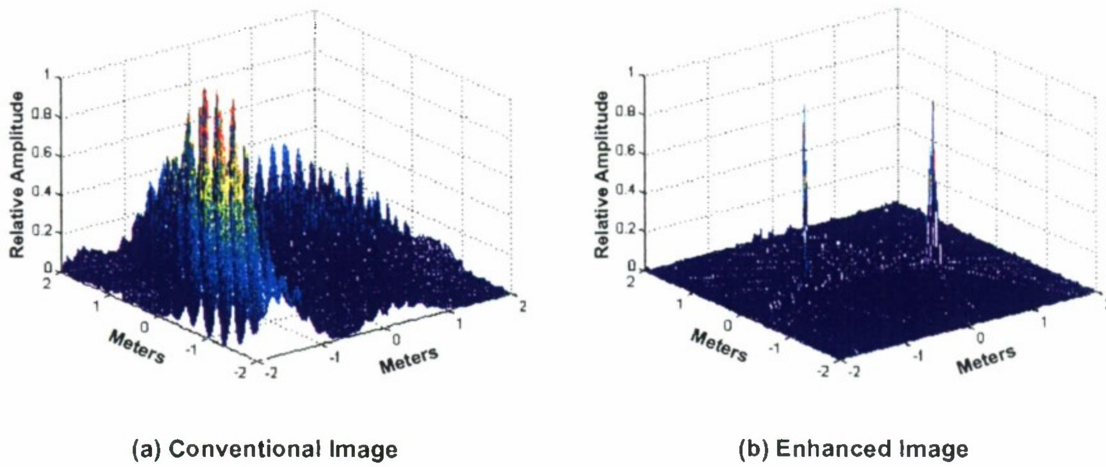

Figure 41. Conventional and enhanced images of two-dimensional strip using fused data (Example 2).

4.3.3 A Three-Dimensional Example

The next example considers perhaps the simplest three-dimensional scattering body that exhibits shadowing and therefore multiple speculars: a right-circular cone. The cone geometry is illustrated in Figure 42(a); the field magnitude over the region 0 to 360 deg is illustrated in Figure 42(b). The cone considered has a length of 2 m, comparable with the strip, and a base diameter of 0.5 m, which produces a half-cone angle of 6.5 deg and leads to a cone specular at $\varphi = 83.5$ deg and $\varphi = 276.5$ deg, along with a base specular at $\varphi = 180$ deg. Typically, the scattering from a sharp nosetip associated with the cone is small; for this reason the nose scattering in the example has been enhanced by a transition to a small spherical nose of radius 0.1 m.

Before proceeding to some specific sensor-fusion examples, it is instructive to examine the functional form of the diffraction-based solution for backscatter from the right-circular cone base developed by Keller [6]. Because of shadowing, the backscatter contribution takes a different form, depending on whether both base edges are visible to the sensor. In the region where the base is visible, the solution takes the form

$$E(f,\varphi) = E_{d_1}(f,\varphi) + E_{d_2}(f,\varphi) \quad , \tag{79}$$

where

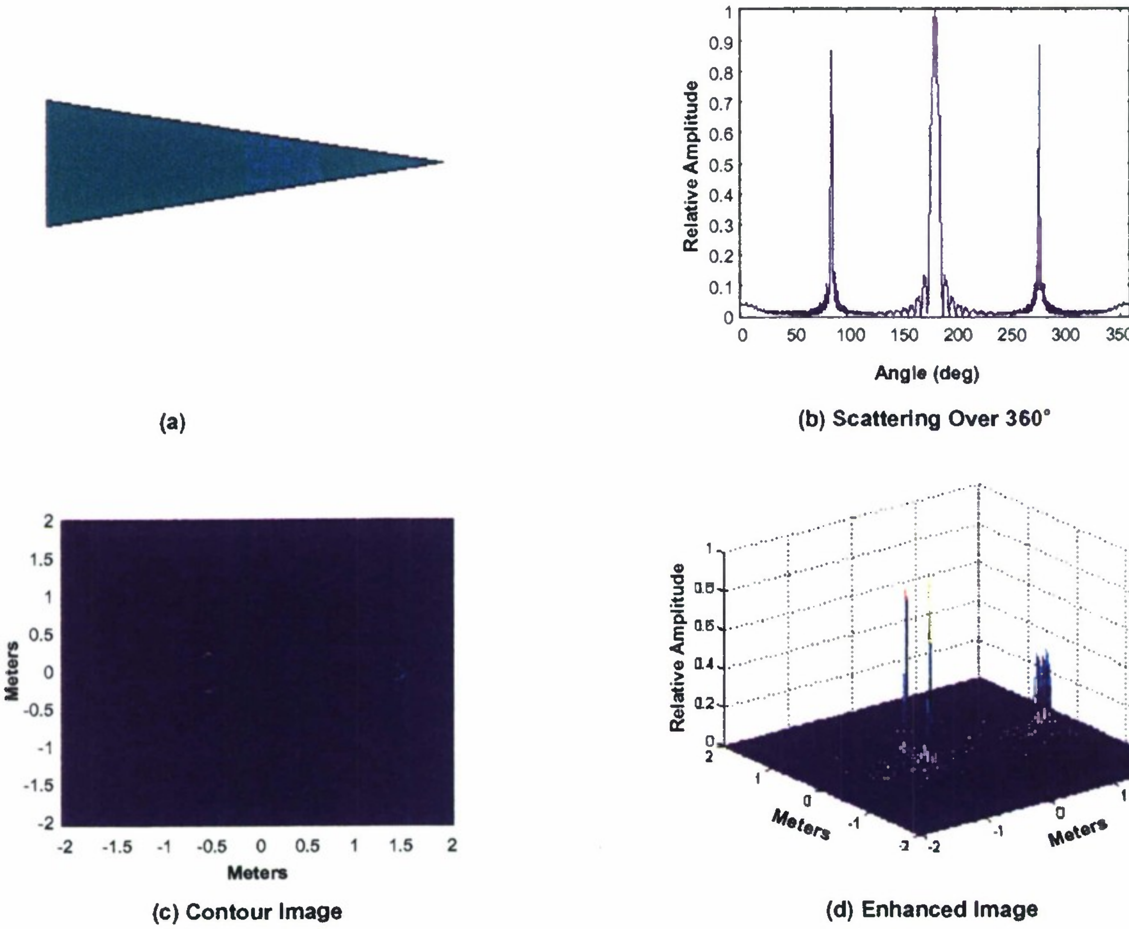

Figure 42. Full-sector enhanced image of right-circular cone.

$$E_{d_1}(f,\varphi) \sim \frac{1}{\sqrt{f\sin\varphi}}\left[C_1 + \frac{C_2}{\sin(\varphi-\pi)}\right]e^{-jux_1}e^{-jvy_1} \quad , \tag{80}$$

and where (x_1,y_1) denotes the location of the upper base edge; $E_{d_2}(f,\varphi)$ is given by Equation (80), with φ replaced by $-\varphi$, and C_1 and C_2 are constants independent of f and φ. Examination of Equation (80) indicates that because of the three-dimensional nature of the base-edge specular (caustic), which occurs at $\varphi = \pi$, the form for the diffraction basis set defined by Equation (55) must be generalized. As the solution to Equation (80) approaches the specular,

$$E_{d_1}(f,\varphi) \sim \frac{1}{\sqrt{f}}\,\frac{1}{\sin^{3/2}(\varphi-\pi)}e^{-jux_1}e^{-jvy_1} \quad , \tag{81}$$

and the field amplitude grows inversely to $\sin^{3/2}(\varphi)$. The validity of this functional form can readily be seen by comparing Equation (81) with the physical optics solution's near-specular:

$$E(f,\varphi) \sim \frac{J_1\left(\frac{4\pi a}{\lambda}\sin\varphi\right)}{\frac{4\pi a}{\lambda}\sin\varphi} \quad . \tag{82}$$

Noting that for $|x|$ large, $J_1(x) \sim \sin(x - 3\pi/4)/\sqrt{x}$, Equation (82) has an envelope consistent with Equation (81) as $\varphi \to \pi$; thus the conclusion that for specular responses from flat surfaces, as opposed to curved specular surfaces such as the cone speculars at $\varphi = 83.5$ deg and $\varphi = 276.5$ deg, the diffraction basis set takes the more general form of Equation (56), with $C_0 = 0$ and $K_2 = 3/2$.

Figure 42(c) illustrates the entire 0- to 360-deg sector-enhanced contour image of the right-circular cone at $(f = 3\ \text{GHz})$, using the cross-range image algorithm defined by Equation (83). The full-sector scattering pattern is illustrated in Figure 42(b), and two views of the enhanced image are shown in Figure 42(c) and Figure 42(d). Observe the variation of the scattering pattern corresponding to each specular off the side of the cone $(\varphi \approx 83\ \text{deg})$ and off the base of the cone. The enhanced image elucidates the presence of the three scattering points, i.e., the base edges and spherical nosetip.

Example 1: Side Specular. Consider now the application of the fusion algorithm defined earlier. Two examples are considered, each restricting the region over which the data are fused to a given specular. For the first example, consider the side specular for which the estimate of φ_s from the "measurement" data set is given by Equation (68). Assume that data are collected by each of two sensors over the sectors given by

$$\begin{array}{l} \text{Sector 1: } (43 \text{ to } 47 \text{ deg}), \quad (\varphi_1 = 45 \text{ deg}) \\ \text{Sector 2: } (73 \text{ to } 77 \text{ deg}), \quad (\varphi_2 = 75 \text{ deg}) \end{array} \quad .$$

Assume further that each sensor is narrowband and operates at $f_0 = 3$ GHz . Figure 43(a) illustrates the "real part" of the known data over each of the sectors; superimposed on this plot is the local all-pole model data fit to each sector. The two results are essentially identical. Applying the source-location estimation algorithm produces the result illustrated in Figure 43(b), from which the base edge and nosetip are clearly evident. Figure 43(c) and Figure 43(d) illustrate the result of fusing and extrapolating these data over a 100-deg sector located over 20 to 120 deg, including the specular region, using only the base edge [Figure 43(c)] and both the nose and the base edge [Figure 43(d)]. Observe that the specular estimate using Equation (68) is quite close to the actual specular and that adding the nose to the base-edge contribution fills in the oscillations in the scattering pattern.

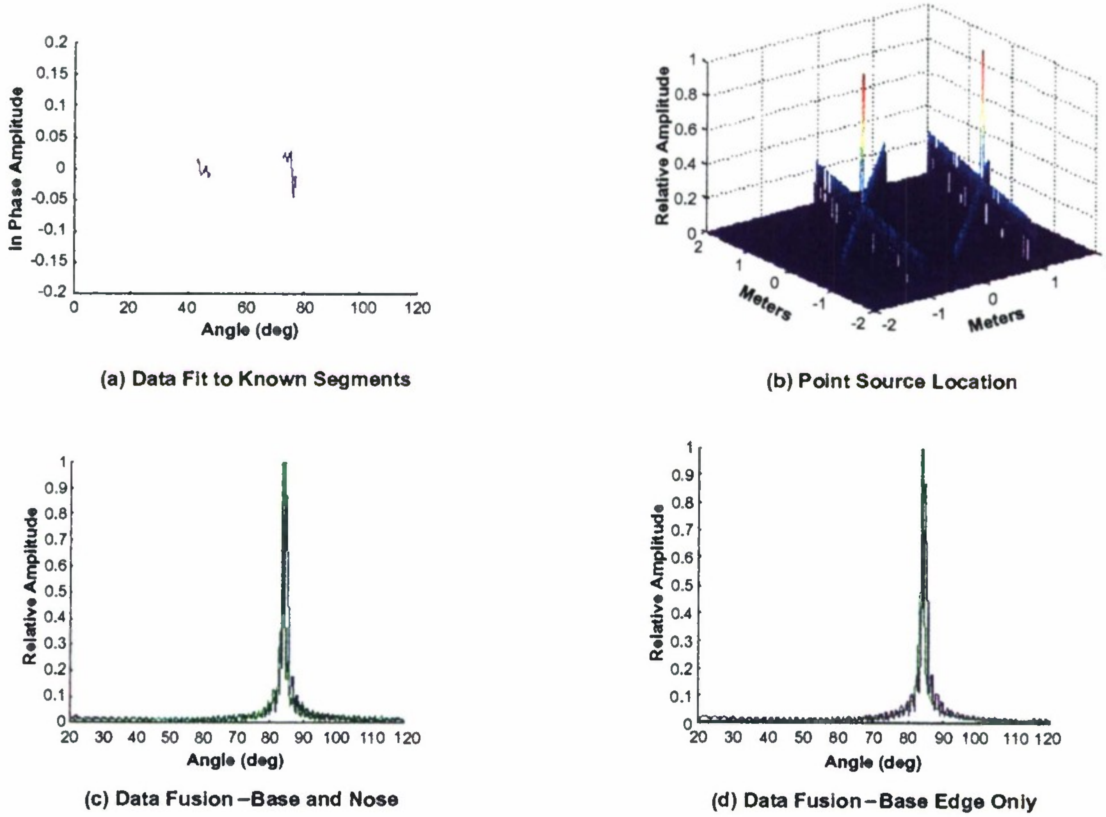

Figure 43. Data fusion for right-circular cone: example 1.

Example 2: Base Specular. For the base specular, the estimate of φ_s given by Equation (68) must change, as Equation (68) is no longer valid for $K = 3/2$. The modified form for Equation (68) for arbitrary K is given by

$$\hat{\varphi}_s \approx \varphi_0 + \tan^{-1}(K/\alpha_m) \quad . \tag{83}$$

If K is known a priori, Equation (83) can be used directly; however, this is generally not the case. For this reason, an alternative algorithm has been developed for estimating both φ_s and K from sparse-angular measurements for the special case where the angular sectors are associated with the same specular. This algorithm could be readily extended to the case of multiple speculars, but as this extension has not yet been done, the examples given are restricted to same-specular examples. The algorithm proceeds as follows: for each subsector under consideration, select the largest-amplitude coefficient from the local all-pole fit to the given data set and characterize the amplitude of this pole by the expression

$$A_s = |A_{\max}| e^{-\alpha_{\max}(\varphi - \varphi_0)} , \tag{84}$$

where $|A_{\max}|$ denotes the largest-amplitude coefficient, $\alpha_{\max}$ denotes the corresponding pole's "real part," and φ_0 is the center of the subsector. This process is carried out for each subsector under consideration, and the data are concatenated into a larger vector string. Denote the concatenated data fit as $\hat{A}(\varphi)$, then choose φ_s and K as the best fit of $D(f_0, \varphi, K, \varphi_s)$ given by Equation (58) to $\hat{A}(\varphi)$ over those regions containing the measurements; i.e.,

$$[K, \varphi_s] = \max_{K, \varphi} \langle |\hat{A}(\varphi) - |D(f_0, \varphi, K, \varphi_s)||^2 \rangle , \tag{85}$$

where the notation $\langle \bullet \rangle$ denotes an average over the known observation angles.

To illustrate this process, consider fusing data associated with the base specular and assume the "measurement" data set is known over four angular sectors given by

Sector 1: (148 to 152 deg), $\varphi_0 = 150$ deg

Sector 2: (158 to 162 deg), $\varphi_0 = 160$ deg

Sector 3: (203 to 207 deg), $\varphi_0 = 205$ deg

Sector 4: (213 to 217 deg), $\varphi_0 = 215$ deg

As in Example 1, assume each sensor is narrowband and operates at $f_0 = 3$ GHz . Figure 44(a) illustrates the "real part" of the known data over each sector; superimposed on this plot is the local all-pole model data fit to each sector. Once again the two results are essentially identical. Figure 44(b) illustrates the results of the source-location estimation algorithm; note that the two base edges are clearly visible and that there is a lower-level indication of the nosetip, along with several ambiguous estimates. Because the nose region is shadowed over most of the base region, the data are fused using only the base-edge locations. The surface generated using Equation (84) for estimating φ_s and K is illustrated in Figure 44(d). The maximum occurs at $\hat{K} \sim 2$ and $\hat{\varphi}_s = 180$ deg; this surface is a weak function of K but is very sharp in estimating φ_s. Using these values, the fused data are illustrated in Figure 44(c), compared with the true data set over the 100-deg region shown.

The value of $\hat{K}$ resulting from the optimization defined by Equation (84) is different than the $K = 1.5$ predicted by Equation (81), although the fit to the data is remarkably good, because of the inability of the two edge scatterers to characterize the specular fully in the immediate region of the large specular response.

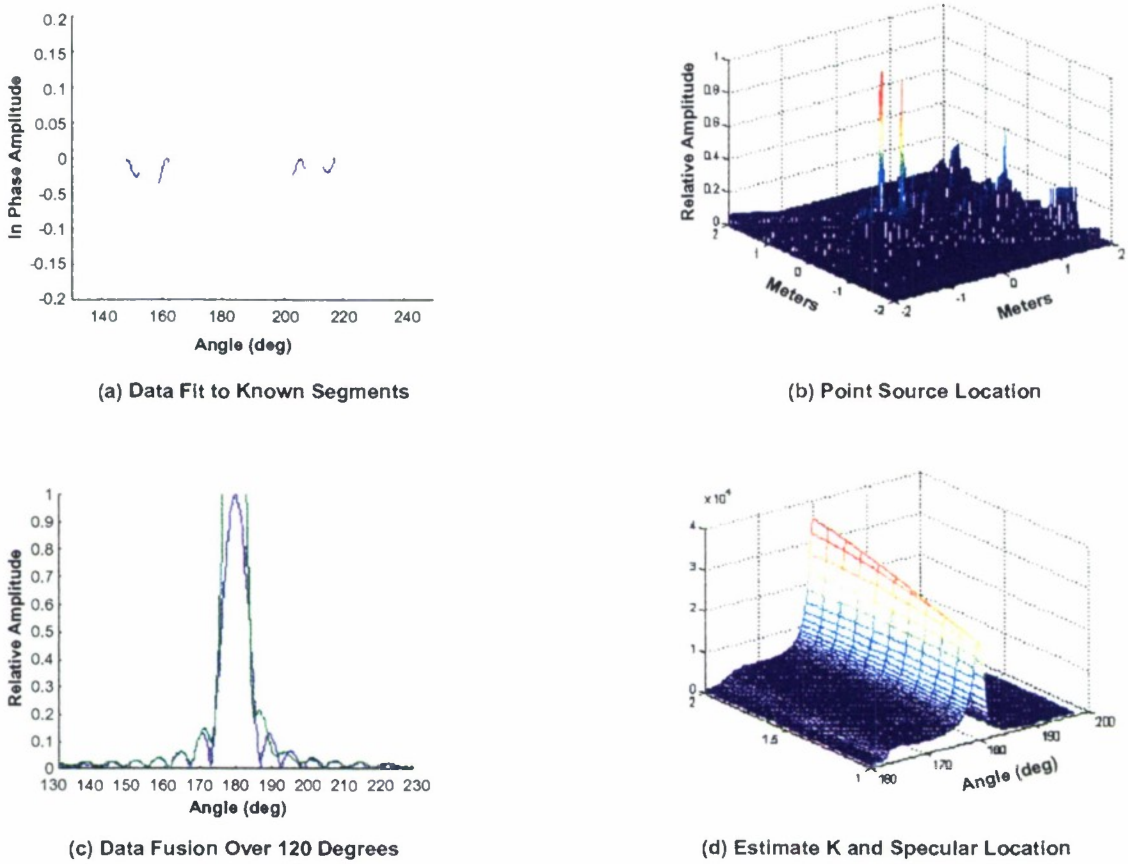

(a) Data Fit to Known Segments

(b) Point Source Location

(c) Data Fusion Over 120 Degrees

(d) Estimate K and Specular Location

Figure 44. Data fusion for right-circular cone: example 2.

4.3.4 Static-Range Data

The examples above illustrate the practicability of the techniques developed on increasingly realistic physical targets. The final example considers applications of these techniques to actual measurement data, using static-range measurement data from the canonical target considered in [1]. The canonical target is illustrated in Figure 45(a): a monoconic model of a reentry vehicle 1.6-m long. The spherical nosetip of the reentry vehicle has a 0.22-cm radius; the nose section is made from a solid piece of machined aluminum with two grooves and one seam. The first groove, which is approximately 3-mm deep and 6-mm wide, is located 22 cm from the nosetip. The second groove is approximately 2-mm deep and 4-mm wide and is located 44 cm from the nosetip. The midbody of the reentry vehicle is made from a single sheet of rolled aluminum with one groove, one slip-on ring, and three seams. The aluminum slip-on ring (not shown in the photo) is approximately 5-mm thick and 10-mm wide and is placed 1.4 m from the nosetip.

Static-range data were measured on this target from 12 to 18 GHz over an angular region from –95 to 95 deg. Figure 45(b) illustrates the radar cross section of the target at 12 and 18 GHz, as indicated in the figure. The data region is wide enough to include the 0-deg nose-on specular that is due to the spherical nosetip and axially symmetric rings, as well as the cone's side specular. Scattering from the side grooves and ring covers a wide dynamic range, as discussed in [1]. This makes a challenging target for the techniques described in this report.

This data-fusion example assumes two narrowband sensors, one at 12 GHz and the other at 18 GHz, each interrogating the target over a 90-deg sector. This example focuses on the source-estimation process, which illustrates that the source-location algorithm developed here is indeed capable of identifying the correct scatterers; characterization of each scatterer and estimation of $D_m(f,\varphi)$ from limited sector data for each source will be the focus of a subsequent report. To estimate the source locations, i.e., to develop a fused image, subdivide the known data region into a sequence of 8-deg subsectors and apply the source-estimation algorithm to this sliding block of data. The measured data and the local all-pole fit to the data as the subsector is incremented in steps of 0.1 deg are illustrated in Figure 46(b). The fused image is illustrated in Figure 46(c) and (d). All the source locations are clearly identified, the large dynamic range notwithstanding. The threshold parameter T_0 defined in Equation (73) is critical to obtaining a large dynamic-range image: essentially it has the effect of reducing the contribution of the very large scatterers.

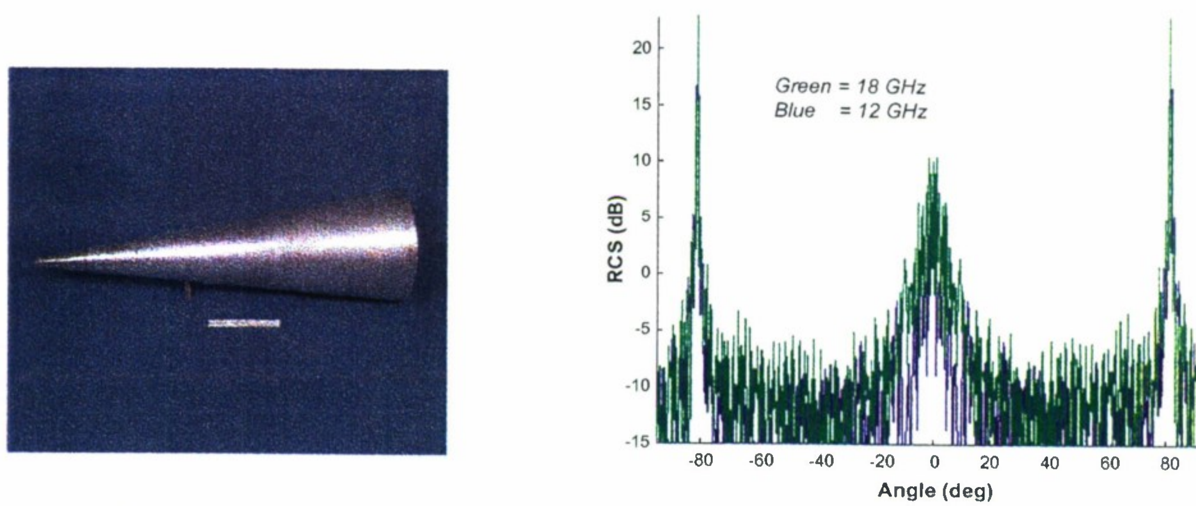

(a) Test Article **(b) Measured Data**

Figure 45. Static-range data on test article.

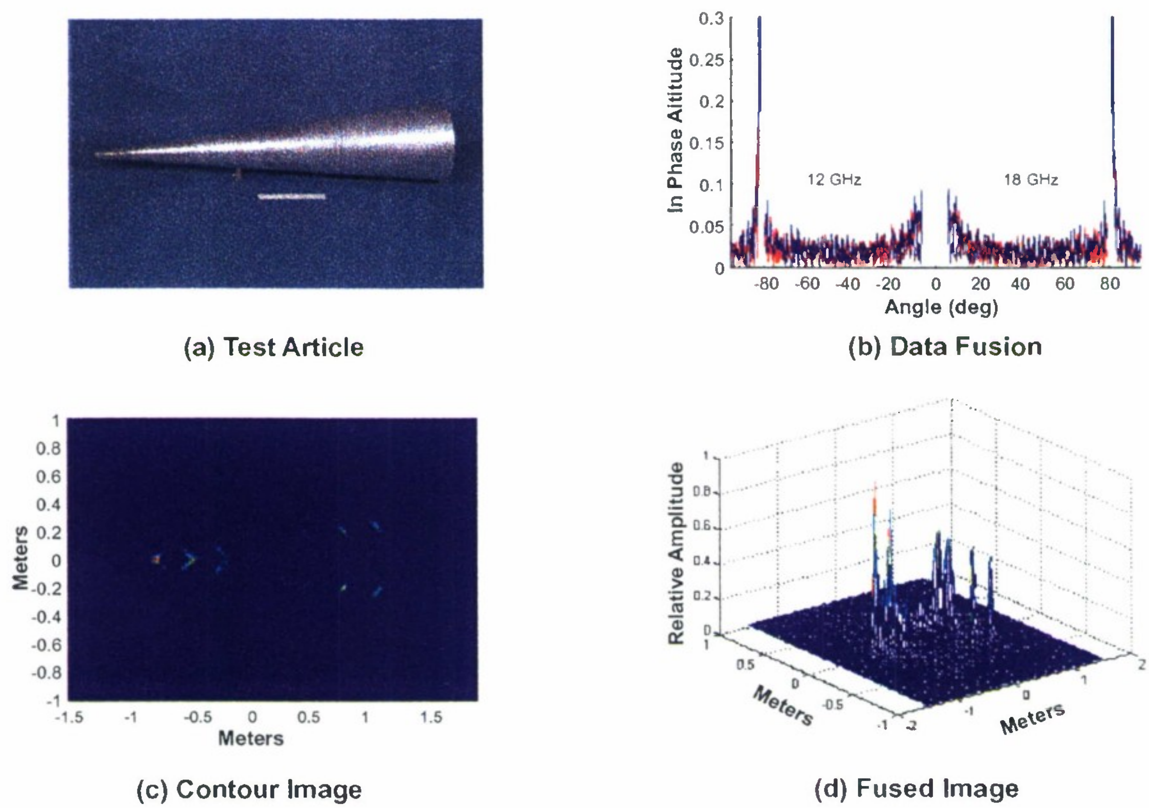

Figure 46. Fused narrowband image of test article.

Figure 47 illustrates the effect of varying the parameter T_0 on the resultant source-location image. A sequence of images is presented for $T_0 = 1.0$, 0.01, 0.001, and 0.0001, respectively, as noted in the figure. Observe that for $T_0 = 1.0$ the base edges and the attached ring dominate the image; as T_0 decreases, the smaller scatterers begin to appear. At $T_0 = 0.0001$ the contributions from each scattering center are essentially equalized.

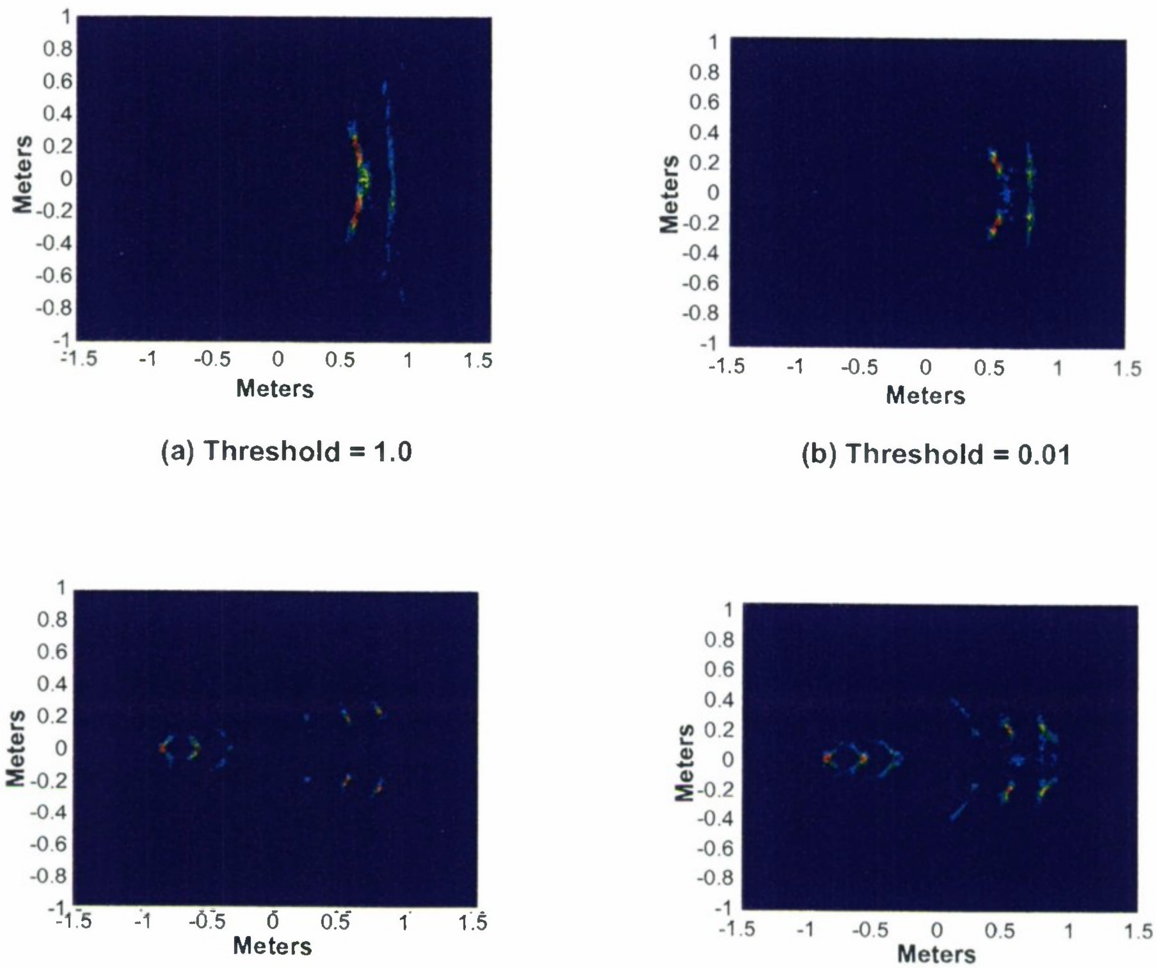

(a) Threshold = 1.0

(b) Threshold = 0.01

(c) Threshold = .0001

(d) Threshold = .001

Figure 47. Effect of variable threshold (18 GHz).

5. COHERENCE EFFECTS

The problem caused by mutual incoherence between the data from sensor 1 and that from sensor 2 is now considered, for which the reader is encouraged to refer back to Figure 3 and Section 1. The problem is examined by considering the example discussed in Section 4.1.1 and illustrated in Figure 15. For simplicity and to illustrate the effects best, consider only the effect of a range-track estimation error (recall Table 1 for the general categories of mutual incoherence). Assume a range-estimation error of 0.1 m for sensor 2 compared with sensor 1. As a result of this range-estimation error, range-delay phase compensations are also in error, and mutual incoherence occurs between data sets. Figure 48 illustrates the image that results from performing ultrawide-bandwidth processing of the S- and X-band data without correction.

A comparison of Figure 23 and Figure 48 shows that significant image degradation results from mutual incoherence between spatially separated sensors; thus, it is essential that data from multiple sensors be mutually coherent before performing ultrawide-bandwidth processing for enhanced radar imaging. The data will be cohered using the method described in [1] before generating an image.

The method used here to cohere the two data sets applies an all-pole model of the form

$$E(f_n) = \sum_{m=1}^{M} a_m p_m^n \tag{86}$$

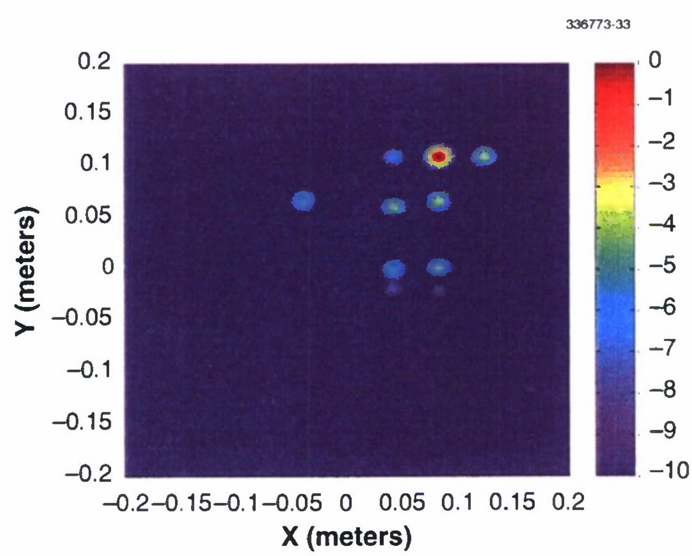

Figure 48. Ultrawide-bandwidth processing of noncoherent data from sensors 1 and 2.

to the data output from sensors 1 and 2. Each pole characterizes the relative range of a scatterer and its frequency-dependence (if its field amplitude varies with frequency). Details of the all-pole modeling technique used in this example can be found in [1]; briefly, the method uses a singular-value decomposition of the forward-prediction matrix for each data set, given by

$$\mathbf{H}_{\mathbf{s1(s2)}} = \begin{bmatrix} s_0 & s_1 & \dots & s_{L-1} \\ s_1 & s_2 & \dots & s_L \\ \cdot & \cdot & \cdot & \cdot \\ \cdot & \cdot & \cdot & \cdot \\ \cdot & \cdot & \cdot & \cdot \\ s_{N-L} & s_{N-L+1} & \dots & s_{N-1} \end{bmatrix} , \tag{87}$$

where $\mathbf{H}_{\mathbf{s1(s2)}}$ has the form of a Hankel matrix whose eigenstructure can be exploited to estimate the parameters of linear time-invariant signal models. The singular-value decomposition decomposes each matrix into the product of three matrices:

$$\mathbf{H}_{\mathbf{s1(s2)}} = \mathbf{U}_{\mathbf{s1(s2)}} \mathbf{S}_{\mathbf{s1(s2)}} \mathbf{V}'_{\mathbf{s1(s2)}} , \tag{88}$$

where the prime symbol denotes the Hermitian operator. The $\mathbf{S}_{\mathbf{s1(s2)}}$ matrices contain the singular values for their respective data sets; the $\mathbf{U}_{\mathbf{s1(s2)}}$ and $\mathbf{V}_{\mathbf{s1(s2)}}$ matrices contain the corresponding eigenvectors. The columns of $\mathbf{V}_{\mathbf{s1(s2)}}$ correspond to the eigenvectors of the covariance matrix for each sensor, and the matrices are used to estimate the model order $P_{s1(s2)}$ for each data set. The estimated model orders $P_{s1(s2)}$ are used to partition $\mathbf{V}_{\mathbf{s1(s2)}}$ into orthogonal signal-plus-noise and noise subspaces. A modified root-MUSIC algorithm is then used to estimate the signal poles for each set of data. The all-pole model amplitude coefficients $a_{m_{s1(s2)}}$ are found using a linear least-squares fit to the data.

Figure 49 shows the resulting pole estimates for the S- and X-band sensor data. Because of the lack of mutual coherence, the X-band signal poles do not line up with S-band signal poles. Coherence is achieved by rotating the X-band poles until they optimally match the S-band poles, which has the effect of phase-aligning the data from both sensors.

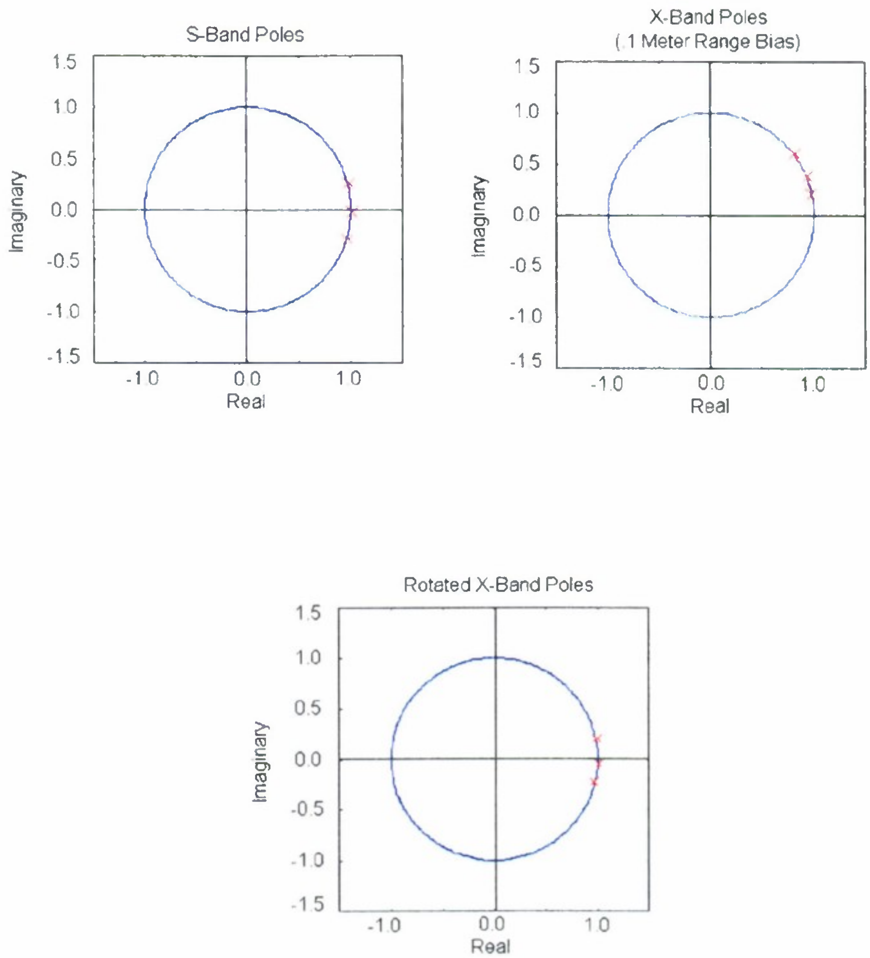

Figure 49. Signal poles of data output from sensor 1 (S-band) and sensor 2 (X-band).

Figure 50 shows the X-band poles that result after rotation to optimally match the S-band poles. The original X-band data, $E(f_n,\varphi)$, is now replaced by mutually coherent data, $\hat{E}(f_n,\varphi)$, given by

$$\hat{E}(f_n,\varphi) = E(f_n,\varphi)e^{j(C_1 + C_2 n)} \quad , \tag{89}$$

where C_1 and C_2 correspond to the X-band pole rotation.

Figure 51 is the image generated from the original S-band data plus the modified X-band data that were generated from the all-pole model after rotating pole locations to match optimally those of the S-band model. A comparison of Figure 23, Figure 48, and Figure 51 clearly shows the importance of mutually cohering multisensor data before generating an image.

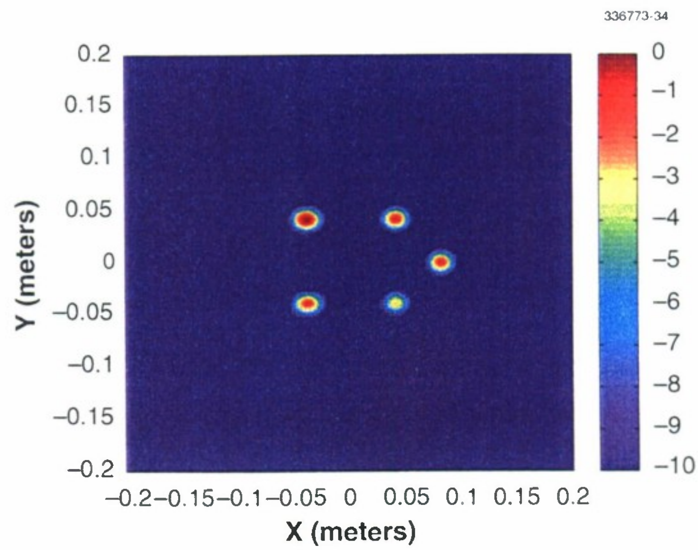

Figure 50. X-band poles after rotation to match S-band poles.

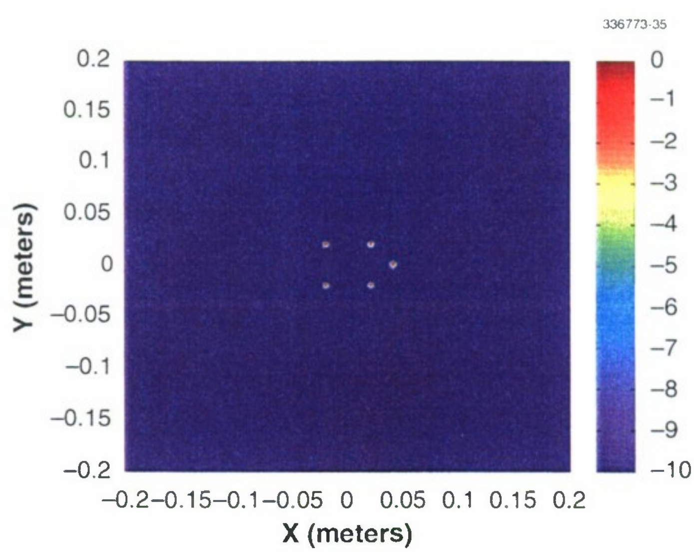

Figure 51. Image from combined sensor data after phase alignment.

6. SUMMARY

There is considerable interest within the ballistic missile defense community for the various theater and area-defense systems to operate as a family of systems. A key ingredient in fully accomplishing this objective is the capability to fuse signature data from a variety of sensors operating over different frequency bands and interrogating a target over diverse angular positions. This report develops (1) a framework for fusing signature data for this diverse operating scenario, (2) candidate sensor-fusion algorithms, and (3) a general formulation characterizing the practical problem of cohering data associated with multiband spatially distributed sensors. The report illustrates the formulation by considering numerous examples, transitioning from simple illustrative targets to progressively more difficult and physically realistic targets. The report begins with a constant-amplitude point-scatter model, progresses to three-dimensional targets, and ends by illustrating enhanced image-fusion algorithms applied to static-range data.

In some sense this report can be considered a complement to the ultrawide-bandwidth development presented in [1], which develops the general formulation for fusing signature data from sparse-band collocated sensors. This report focuses primarily on the complementary problem of sparse-angle sensor fusion, where three main effects complicate the fusion process: specular responses, diffraction from discontinuities, and shadowing. These effects prohibit the use of a constant-amplitude point-scatter model for characterizing the target over broad angular regions, which is clearly evident from the geometrical theory of diffraction, where Equation (51) elucidates the complex-amplitude variation $D_m(f,\varphi)$ required to characterize a given discontinuity.

For the constant-amplitude point-scatter model, it is possible to develop a two-dimensional wideband all-pole formulation for fusing sparse-angle multiband data by transforming the problem from (f,φ) space to (u,v) space, as defined in Equation (13); in the general case, however, the diffraction coefficient $D_m(f,\varphi)$ is not readily characterized in (u,v) space. To circumvent this problem, a new basis-expansion set was developed based on the diffraction from a wedgelike discontinuity and generalized to a broader class of discontinuities, as illustrated in Figure 32. Use of this basis set allows the use of a localized all-pole model over a limited angular sector and the fusion of these data using the generalized expansion defined by Equation (65) and Equation (66). A candidate fusion algorithm was developed and described in Section 4.3.2 and was then applied to numerous examples.

A striking duality was demonstrated between sensor coherence for sparse-band collocated sensors and sparse-angle narrowband sensors; this duality is summarized in Figure 14. For collocated sensors, range-bias errors lead to an offset of the wideband pulse processed by each sensor. If these pulses are combined without compensating for the range-bias error, the relative position of the scatterers indicated by the wideband compressed pulse do not match, resulting in misidentification of the number of scattering centers. The locations of these scatterers for each subband are characterized by a pole plot for each subband spectral estimate and the pole-rotation angle, which causes the respective subband pole estimates to coalesce into one that characterizes the delay and range-bias errors. Analogously, for narrowband sensors with different look angles to the target, processing each subsector leads to a cross-range profile of the target. If these cross-range profiles are lined up without angle-bias compensation, common scattering points do not coincide, and once again a misidentification of scattering centers occurs.

The above discussion can be easily extrapolated to the general case of two wideband sensors located at different angular positions. Each sensor is capable of forming an image of the target, with image quality dependent on subbandwidth (range resolution) and angular sector size (cross-range resolution). Proper multisensor fusion allows coherent combination of these images, for improved image quality. Range- and system-delay mismatches between sensors result in "range" misalignment of each image, angle-bias errors result in cross-range misalignment, and phase errors result in less coherent processing gain in combining corresponding image points. Coherent signature fusion can be accomplished only when sensors are mutually cohered to eliminate these misalignments and phase errors.

REFERENCES

1. K.M. Cuomo, J.E. Piou, and J.T. Mayhan, "Ultra-Wideband Coherent Processing," *IEEE Trans. Antennas Propag.*, 47, 1094–1107 (1999).

2. D.L. Mensa, *High-Resolution Radar Imaging*, Lexington, Mass.: Artech House (1981).

3. T.G. Moore, B.W. Zuerndorfer, and E.C. Burt, "Enhanced Imagery Using Spectral-Estimation–Based Techniques," *Lincoln Lab. J.*, 10, 171–187 (1997).

4. D.W. Duan, Y. Rahmat-Samii, and J.P. Mahan, "Scattering from a Circular Disk: A Comparative Study of PTD and GTD Techniques," *Proc. IEEE*, 79, 1472–1480 (1991).

5. W.M. Steedly and R.L. Moses, "High-Resolution Exponential Modeling of Fully Polarized Radar Returns," *IEEE Trans. Aerosp. Electron. Sys.*, 27, 459–469 (1991).

6. J.B. Keller, "Backscattering from a Finite Cone," *IEEE Trans. Antennas Propag.*, March, 175–182 (1960).

REPORT DOCUMENTATION PAGE

Form Approved OMB No. 0704-0188

1. AGENCY USE ONLY (*Leave blank*)	2. REPORT DATE	3. REPORT TYPE AND DATES COVERED
	5 April 2000	Technical Report

4. TITLE AND SUBTITLE

Multisensor Fusion Processing for Enhanced Radar Imaging

5. FUNDING NUMBERS

C — F19628-95-C-0002

6. AUTHOR(S)

Laura D. Vann, Kevin M. Cuomo, Jean E. Piou, and Joseph T. Mayhan

7. PERFORMING ORGANIZATION NAME(S) AND ADDRESS(ES)

Lincoln Laboratory, MIT
244 Wood Street
Lexington, MA 02420-9108

8. PERFORMING ORGANIZATION REPORT NUMBER

TR-1056

9. SPONSORING/MONITORING AGENCY NAME(S) AND ADDRESS(ES)

U.S. Army Space and Missile Defense Command
P.O. Box 1500
Huntsville, AL 35805

10. SPONSORING/MONITORING AGENCY REPORT NUMBER

ESC-TR-99-059

11. SUPPLEMENTARY NOTES

None

12a. DISTRIBUTION/AVAILABILITY STATEMENT

Approved for public release; distribution is unlimited.

12b. DISTRIBUTION CODE

13. ABSTRACT (*Maximum 200 words*)

This report considers the problem of fusing signature data from a variety of sensors operating over different frequency bands and interrogating a target over diverse angular positions. In particular, the report develops: 1) a framework for fusing signature data for this diverse operating scenario, 2) candidate sensor-fusion algorithms, and 3) a general formulation characterizing the practical problem of cohering data associated with multiband spatially distributed sensors. The report illustrates the formulation by considering numerous examples, transitioning from simple illustrative targets to progressively more difficult and physically realistic targets. The report begins with a constant-amplitude point-scatter model, progresses to three-dimensional targets, and ends by illustrating enhanced image-fusion algorithms applied to static-range data.

14. SUBJECT TERMS

Combat ID
ISAR imaging
Multiband processing
Sensor fusion
Angle diversity
Target identification

15. NUMBER OF PAGES

81

16. PRICE CODE

17. SECURITY CLASSIFICATION OF REPORT	18. SECURITY CLASSIFICATION OF THIS PAGE	19. SECURITY CLASSIFICATION OF ABSTRACT	20. LIMITATION OF ABSTRACT
Unclassified	Unclassified	Unclassified	Same as Report